Experimental observation of non-Abelian topological charges and edge states

SUPPLEMENTARY INFORMATION for "Experimental observation of non-Abelian topological charges and edge states"

Qinghua Guo, Tianshu Jiang, Ruo-Yang Zhang, Lei Zhang, Zhao-Qing Zhang, Biao Yang, Shuang Zhang, C. T. Chan

Contents

I.   Understand non-Abelian topological charges

Understanding quaternion charge from rotation matrix

We start with employing the rotation matrix to build an ideal real Hamiltonian for the three-band system. Generally a Hermitian Hamiltonian can be constructed by $H(k) = \sum_{n=1}^{N} \lambda_n |u_k^n\rangle\langle u_k^n|$, where we assume no band degeneracy and thus $\lambda_1 < \lambda_2 < \cdots < \lambda_N$. Each eigenvalue λ_n corresponds to a single eigenstate $|u_k^n\rangle$, i.e. $H(k)|u_k^n\rangle = \lambda_n|u_k^n\rangle$. Furthermore, spectral theorem says that any Hermitian matrix can be written as $H(k) = U(k)\Lambda(k)U(k)^\dagger$ ('$\dagger$' combines both complex conjugate '$*$' and transpose 'T') with $\Lambda(k) = diag(\lambda_1, \lambda_2, \dots, \lambda_N)$ being diagonal and real, where $U(k)$ is a unitary matrix consisting of (ordered) orthonormal eigenstates $|u_k^n\rangle$. In our PT symmetric system, the Hamiltonian can take real symmetric form and thus the unitary matrix $U(k)$ reduces to be real rotation matrix $R(k)$. On the other hand, we make $\lambda_n = n$ to further simplify the analytical calculation without changing the underlying topological arguments. Thus, the real symmetric Hamiltonian takes the simple form of $H(k) = R(k)diag(1,2,\dots,N)R(k)^T$. When $k = -\pi \to \pi$ runs across the first Brillouin zone, $R(k)$ serves to rotate the eigenstate of each band from an initial state $|u_k^n\rangle = (0,\dots,\underset{n}{\underbrace{1}},\dots,0)$ with only the nth entry being 1. For the non-Abelian charges $+i/+j/+k$, two of three eigenstates rotate π ($|u_k^n\rangle \to -|u_k^n\rangle$) when $k = -\pi \to \pi$ spanning the 2π range, which can be expressed by $R(k) = \exp\left[\frac{(k+\pi)}{2}L_i\right]$ ($i = x,y,z$) with $(L_i)_{jk} = -\epsilon_{ijk}$ and ϵ_{ijk} being the fully antisymmetric tensor. For the charge -1, two of three eigenstates rotate 2π ($|u_k^n\rangle \to |u_k^n\rangle$) when $k = -\pi \to \pi$ spanning the 2π range, which gives $R(k) = \exp[(k+\pi)L_i]$ ($i = x,y,z$). Thus, when $k = -\pi$ the rotation matrix is a $N \times N$ unit matrix $I_{N\times N}$, i.e., $R(k = -\pi) = \exp\left[\frac{(-\pi+\pi)}{2}L_i\right] = I_{N\times N}$ ($i = x,y,z$). Actually, different non-Abelian topological charges will

have different rotation matrices $R(k)$. In other words, the rotation matrix $R(k)$ carries the underlying topological characters and determines the non-Abelian topological charges.

It is worth noting that in general, the winding trajectories of eigenstates in Figs. 1b-e of the main text are not fixed on the great circles. In contrast to which axis the states wind about, the crucial property of $\pm i/\pm j/\pm k$ topological phases is that the trajectories of two of the three bands must terminate at pairs of antipodal points on the eigenstate-frame sphere, which prohibits the trajectories from contracting to isolated points. And the difference of $\pm i/\pm j/\pm k$ phases is reflected by which two bands are noncontractible.

Understanding the order-parameter space M_3

The order-parameter space of Hamiltonian of the three-band model can be written as $M_3 = \frac{O(3)}{O(1)^3} \cong \frac{SO(3)}{D_2}$ [1,2], where the first equality is obtained by an $O(3)$ rotation of the eigenstate frame. As flipping the sign of each eigenstates $|u_k^n\rangle \to -|u_k^n\rangle$ ($n = 1,2,3$) leaves the Hamiltonian $H(k) = \sum_{n=1}^N \lambda_n |u_k^n\rangle\langle u_k^n|$ invariant, one then imposes the $O(1)^3$ quotient, where $O(1)^3 \cong D_{2h} \cong \mathbb{Z}_2^3$ is generated by three mutually perpendicular mirror symmetries. In the second equality, both groups have been replaced by their proper subgroups, i.e., $O(3) \to SO(3)$ and $D_{2h} \to D_2$, where the dihedral point group D_2 consists of the identity and three π rotations around three mutually perpendicular axes.

The special orthogonal group $SO(3)$ can be further parameterized as a solid sphere, wherein the normalized vector $\vec{n} = (n_x, n_y, n_z)$ indicates the rotation axis and radius is rotation angle $\phi \in [0, \pi]$. It is worth noting that the antipodal points $(\vec{n}, \pi)$ and $(-\vec{n}, \pi)$ represent the same

rotation and thus are identical. When k runs from $-\pi$ to π, $R(k)$ traces out a curve in the space of $SO(3)$. On the other hand, one can form the topological space X/H with identifying points of X which can be related by some element of H ($x \equiv xh$), where $x \in X$ and $h \in H$. For the above coset space $\frac{SO(3)}{D_2}$, the D_2 quotient further generates each element $R(k) \in SO(3)$ to be four elements as $R(k) \circ g$ where $g \in D_2 = (I, C_{2x}, C_{2y}, C_{2z})$. If $R(k) \in SO(3)$, then the trajectories of $R(k: -\pi \to \pi) \circ D_2$ represent the four curves in the $SO(3)$ parameter space. For different non-Abelian charges, the curves shown in Figs. S1a-d correspond to Figs. 1b-e in the main text, respectively. Although one single curve cannot connect a pair of antipodal points on the parameterized solid sphere of $SO(3)$, two curves connected together are terminated at the antipodal points as shown in Fig. S1. For example, the green and blue (red and black) curves in Fig. S1a for charge $+i$ thread a pair of antipodal points, they are hence closed and not contractible, which is topologically guaranteed by $\pi_1(SO(3)) = \mathbb{Z}_2$. However, for the charge of -1 as shown in Fig. S1d, one single curve connects a pair of antipodal points because when k running across the first Brillouin zone the rotation $R(k)$ goes from $(\vec{n}, 0) \to (\vec{n}, \pi) \to (\vec{n}, 2\pi) \equiv (\vec{n}, 0)$ as indicated by the black curve.

In Fig. S2 we further show the continuous transition of charge -1 in $SO(3)$ space, where the arcs in Fig. S2b always thread pairs of antipodal points, indicating that the eigenstate trajectories (Fig. S2a) cannot be contractible simultaneously. It is worth mentioning that the rotation axis does not need to lie in the $x - z$ plane. In other words, the green eigenstate trajectory does not have to be the great circle. More generally, if the rotation axis is away from the three central planes (i.e., $x, y, z = 0$), no trajectory would be great circle. Certainly, they still cannot be contractible simultaneously.

Zak phase perspective of quaternion charge

For a single bandgap system (or we only focus on a single bandgap while ignoring other bandgaps, in other words other bandgaps may close at will), the topological phase protected by PT symmetry is $\mathbb{Z}_2$ classified (with more than two bands). It means that the bandgap may have Zak phase taking values of 0 and $\pm\pi$, where $\pm\pi$ refer to the same phase with mod of 2π. Thus, no topological domain-wall state is guaranteed to exist on the domain-wall between $+\pi$ and $-\pi$. *(Note that in this work the term "edge" can be generalized to be "domain-wall" when considering both two charges $Q_L \neq 1$ and $Q_R \neq 1$. Instead, an edge can be viewed as a domain-wall between a crystal and vacuum or hard-wall.)*

In the non-Abelian topological system with three bands separated by two bandgaps, if we label each band with Zak phase, there are $2^{n-1} = 4$ (the total number of bands $n = 3$) possibilities. Because each band can take two values, 0 or $\pm\pi$ ($\pm\pi$ *are the same with mod of* 2π), and the sum of all Zak phases $\sum_{n=1}^{3} \phi_n = 0 \ (mod \ 2\pi)$ imposes that only $n - 1$ bands are independent. However, the non-Abelian topological charge $\mathbb{Q}$ has 5 conjugacy classes $(+1, \pm i, \pm j, \pm k, -1)$. Therefore, the class -1 goes beyond the Zak phase description[1]. In Fig. 4c we label it as 2π to make the distinction between it and the trivial class $+1$. Note that[1] a 2π frame rotation does not imply that the Zak phase of charge -1 is 2π, which is the case only in some special configurations when one of bands is fully decoupled and the other two bands can be classified by $\mathbb{Z}$ for the PT symmetric system. For other conjugacy classes, each has the unique Zak phase distribution. Between two different classes, the Zak phases $+\pi$ and $-\pi$ are topologically equivalent being consistent to the usual arguments in the Abelian topological phases. But, in a single conjugacy class, we apply them two to distinguish two distinct elements. For example, we label the 1st/2nd bandgap of charge $\pm i$ with $0/\pm\pi$ (as shown in Fig. 4c in

the main text). It is due to that in each conjugacy class the two elements (i.e. $+i$ and $-i$) have a relative meaning, i.e., representing the two opposite rotations of the eigenstate frame when k running across the first Brillouin zone ($k = -\pi \to \pi$). It is worth stressing that although the two charges $+i$ and $-i$ belong to one conjugacy class, they are still two topologically distinct charges as their transition has to induce bandgap closing (given a common basepoint). Furthermore, there are two linear Dirac cones during the transition (as shown in Fig. S9d). Thus, the domain-wall between $+\pi$ and $-\pi$ of charges $+i$ and $-i$ supports two topological domain-wall states, just like the edge states of charge -1 (Fig. S11d with $\theta_z \to 0$). On the other hand, according to our non-Abelian quotient relation, the relation $\Delta Q = +i/-i = -1$ implies that the domain-wall of charge pair $(+i, -i)$ supports similar edge states of charge -1 with a hard boundary. Finally, the two arguments are consistent.

Understanding the conjugacy class of quaternion group

The quaternion group $\mathbb{Q}$ has five conjugacy classes ($+1, \pm i, \pm j, \pm k, -1$) in total and three of them contain two conjugate elements, i.e., $\pm i$, $\pm j$ and $\pm k$. In the Abelian topological charge group, such as $\mathbb{Z}$ and $\mathbb{Z}_2$, each element is a class by itself. However, in the non-Abelian topological charge group one class may contain several elements. Thus, conjugacy class is special to the non-Abelian topological phases. Elements of the same conjugacy class cannot be distinguished by using only the group structure and therefore share many similar features. However, it does not mean that the two conjugate elements are the same. In the non-Abelian topological phases one cannot continuously transform charge $+i$ to $-i$ without gap closing given a common basepoint (see Fig. S9d).

Calculating non-Abelian topological charges

In this work we follow Ref.[1] to calculate the non-Abelian topological charges. The generalized Wilson operator can be written as,

$$W_I(\Gamma) = \exp[\oint A_{all}(k) \cdot dk] \tag{S1}$$

where $[A_{all}(k)]_{n\alpha}^m = \langle u_k^m | \partial_{k_\alpha} | u_k^n \rangle$ being anti-symmetric under PT symmetry is a $\mathfrak{so}(N)$-valued 1-form. m and n are the band indices which cover all of bands to obtain the affine Berry-Wilczek-Zee (BWZ) connection. We first decompose the affine BWZ connection into the $\mathfrak{so}(N)$ basis as,

$$[A_{all}(k)]_\alpha = \sum_n \beta_\alpha^n(k) L_n \tag{S2}$$

and then lift it onto the $\mathfrak{spin}(N)$-valued 1-form as,

$$[\bar{A}_{all}(k)]_\alpha = \sum_n \beta_\alpha^n(k) t_n \tag{S3}$$

where the basis element t_n is defined as $t_n = -\frac{i}{2}\sigma_n$ with σ_n being Pauli matrix. The generalized quaternion charge acquired along a closed loop can be expressed as,

$$Q = \exp[\oint \bar{A}_{all}(k) \cdot dk] \tag{S4}$$

Finally, we discretize the integration (Eq. S4) and obtain the non-Abelian charge. The quaternion group elements are represented as $1 \to \sigma_0$, $i \to -i\sigma_x$, $j \to -i\sigma_y$ and $k \to -i\sigma_z$, where σ_0 is the 2×2 identity matrix.

II.   Continuous transition in the charge -1

The singularity of charge -1 is schematically illustrated in Fig. S3a, where red and green vectors rotate 2π around the centre while the blue ones pointing upwards. After applying a continuous local gauge field, one can smoothly map the triad-vector field onto a semi-sphere as shown in Fig. S3b. During the mapping, the singularity point remains intact and thus the

topology is well preserved. We then increase the cyan loop radius in Fig. S3b. Finally, we find that along the cyan loop the red vectors almost remain fixed while the other two rotate 2π as shown in the right panel of Fig. S3c.

When we rotate the cyan loop from Fig. S3d to f, the topological charge changes from -1 to $+1$, where the singularity goes out the cyan loop. Obviously, the trajectories of three eigenstates are contractible for the charge $+1$ as shown in Fig. S3g.

The topological features illustrated in Fig. S3 are closely related to the topology of the eigenmodes in our multi-band system. The red/green/blue vectors in these figures correspond to the eigenstates of the 1st /2nd /3rd band in our multi-band system. The cyan loops correspond to the 1D first Brillouin zone, along which the eigenstates of a "1D Hamiltonian" rotate as shown in Figs. S3c, e and g. Different panels in Fig. S3c represent different configurations of the charge -1. But we can see from Figs. S3a and b that they are all topologically equivalent, as they all correspond to a loop (cyan loop) encircling the same singularity point. In the later Secs. VI and VII (Figs. S15-S19) we propose a systematic way of extending the 1D Hamiltonian onto an extended 2D plane. Based on the degeneracy details of 2D band dispersions, we predict the edge state distributions of the 1D Hamiltonian for different quaternion charges.

III.   Tight binding model and edge states

The real-space Hamiltonian reads (Fig. S4),

$$\mathcal{H} = \sum_n \begin{pmatrix} \sum_{\substack{X=A,B,C \\ Y=A,B,C}} s_{XY} c_{X,n}^\dagger c_{Y,n} + \\ \sum_{\substack{X=A,B,C \\ Y=A,B,C}} v_{XY} c_{X,n}^\dagger c_{Y,n+1} + \sum_{\substack{X=A,B,C \\ Y=A,B,C}} v_{XYl} c_{X,n}^\dagger c_{Y,n+2} + h.c. \end{pmatrix} \tag{S5}$$

where $c_{X,n}^\dagger$ and $c_{X,n}$ are creation and annihilation operators on the sub-lattice 'X/Y' and site 'n', respectively. Here, we consider a more general case having both the NN (nearest neighbour) and NNN (next-nearest neighbour) hoppings. After Fourier transformation we obtain,

$$H(k) = \begin{bmatrix} s_{AA} + 2v_{AA}\cos k & 2u\sin k & 2w\sin k \\ 2u\sin k & s_{BB} + 2v_{BB}\cos k & 2v\sin k \\ 2w\sin k & 2v\sin k & s_{CC} + 2v_{CC}\cos k \end{bmatrix}$$

$$+ \begin{bmatrix} 2v_{AAl}\cos 2k & 2u_l\sin 2k & 2w_l\sin 2k \\ 2u_l\sin 2k & 2v_{BBl}\cos 2k & 2v_l\sin 2k \\ 2w_l\sin 2k & 2v_l\sin 2k & 2v_{CCl}\cos 2k \end{bmatrix}$$

$$+ \begin{bmatrix} 0 & s_{AB} + 2r\cos k & s_{AC} + 2q\cos k \\ s_{BA} + 2r\cos k & 0 & s_{BC} + 2p\cos k \\ s_{CA} + 2q\cos k & s_{CB} + 2p\cos k & 0 \end{bmatrix}$$

$$+ \begin{bmatrix} 0 & 2r_l\cos 2k & 2q_l\cos 2k \\ 2r_l\cos 2k & 0 & 2p_l\cos 2k \\ 2q_l\cos 2k & 2p_l\cos 2k & 0 \end{bmatrix} \tag{S6}$$

where we have set $v_{AB} = r + iu = v_{BA}$, $v_{BC} = p + iv = v_{CB}$, $v_{CA} = q + iw = v_{AC}$, $v_{ABl} = r_l + iu_l = v_{BAl}$, $v_{BCl} = p_l + iv_l = v_{CBl}$ and $v_{CAl} = q_l + iw_l = v_{ACl}$. The red parts will only be used when calculating edge state evolution of charge -1 (Fig. S11). Ignoring the red parts of the Hamiltonian, there is a total of 15 variables.

We then write the above Hamiltonian in the form as,

$$H(k) = R(k)diag(1,2,3)R(k)^T \tag{S7}$$

When we set $R(k) = e^{\pm\frac{k+\pi}{2}L_{x,y,z}}$, the tight binding model (Eqs. S5-S6) only involves NN hoppings and we can find the 9 coefficients as listed in the Tab. S1, where the corresponding

non-Abelian topological charges are given as well. When we set $R(k) = e^{(k+\pi)L_z}$, the lattice only involves NNN hoppings, the corresponding coefficients of charge -1 are given in the last row of Tab. S1. The four non-Abelian topological charges of $+i$, $+j$, $+k$ and -1 correspond to Figs. 1b-e in the main text, respectively.

The parameters used in the transmission line experiments are given in Tab. S2. Figure S5 shows the corresponding edge states at hard boundaries.

We divide all cases of charge $+j$ into two categories. The first one (as shown in Fig. 2c) is a special case in which the 2nd band is fully decoupled from other two bands. We may neglect the 2nd band and consider the whole bandgap carrying Zak phase of π. Thus, the system supports 1 edge state per edge (2 edge states in total) accordingly. The other case is the general case in which the 2nd band cannot be fully decoupled (as shown in Figs. 3e-f and Fig. S5b), there are two bandgaps where each one carries Zak phase of π, and thus each bandgap supports 1 edge state per edge (4 edge states in total, including two bandgaps and two edges). We show the transition between the two cases, i.e., from decoupling to coupling of the 2nd band in Fig. S6. Basically, we see one extra edge state (per edge) appears after turning on the coupling as shown in Fig. S6. In other words, the total number of edge states changes from two to be four, two of them emerge from middle bulk states when δu increases from 0. In Fig. S6b, we shift the 2nd band away from $E = 2$ to more explicitly show the phenomena.

The edge states of charge $+i/+k$ always stably locate in the 2nd/1st bandgap. We calculated a disordered system as shown in Fig. S7a/b to exhibit the robustness of the edge states against disorder for charge $+i/+k$, as long as both two bandgaps are not closed by the disorder.

Table S1. Coefficients of tight binding model ideally (flat-band) realizing non-Abelian topological charges

Q	s_{AA}	s_{BB}	s_{CC}	v_{AA}	v_{BB}	v_{CC}	u	v	w
$+i$	1	5/2	5/2	0	1/4	-1/4	0	1/4	0
$-i$	1	5/2	5/2	0	1/4	-1/4	0	-1/4	0
$+j$	2	2	2	1/2	0	-1/2	0	0	-1/2
$-j$	2	2	2	1/2	0	-1/2	0	0	1/2
$+k$	3/2	3/2	3	1/4	-1/4	0	1/4	0	0
$-k$	3/2	3/2	3	1/4	-1/4	0	-1/4	0	0

Q	s_A	s_B	s_C	v_{AAl}	v_{BBl}	v_{CCl}	u_l	v_l	w_l
-1	3/2	3/2	3	-1/4	1/4	0	-1/4	0	0

Table S2. Coefficients of tight binding model used in the transmission line experiment

Q	s_{AA}	s_{BB}	s_{CC}	v_{AA}	v_{BB}	v_{CC}	u	v	w
$+i$	0	0	-4	-1	1	0	-1	1	0
$+j$	0	0	0	-1	1	0	-1	1	0
$+k$	0	0	4	-1	1	0	-1	1	0
-1	0	0	0	-1	0	2	-1	1	0

IV. Non-Abelian topological phase transition

With PT symmetry preserved, topological phase transition between different non-Abelian topological charges has to experience bandgap closing. Here we first show the transition from charge $+i$ to $+j$ via changing s_{CC} as shown in Fig. S8. With continuously increasing s_{CC} from -2.2 to -1.8, the bandgap is found to be closed at -2, where the two lower bands linearly cross each other at $k = \pm\pi$ (Fig. S8a). It is consistent with our usual understanding of topological phase transition via bandgap closing and re-opening. It is worth noting that the quadratic degeneracy at $k = 0$ is accidental without any topological consequences. From the eigenstate frames (Fig. S8b), we further see the details of the transition. In particular, at the

gapless points $k = \pm\pi$ two eigenstates are overlapped (indicated by two gray circles in the middle panel of Fig. S8b).

The non-Abelian topological phase transitions can occur between two arbitrary charges. For the Abelian topological phase transitions, one only needs to focus on a single bandgap, whose closing-reopening process implies one topological phase transition. However, in the non-Abelian topological systems, there are multiple bandgaps involved, they may close-reopen individually or simultaneously. For example, the topological phase transition from $+i/+j/+k$ to $+1$ requires for the closing-reopening of the 2nd/(1st and 2nd)/1st bandgap(s) as shown in Figs. S9a-c. We also note that the nontrivial phase transitions between two charges Q_1 and Q_2 with $\Delta Q = Q_1/Q_2 \neq -1$ have one Dirac-cone like crossing (Figs. S9a-c), while the case $\Delta Q = -1$ implies two Dirac cones as shown in Fig. S9d between charges $+i$ and $-i$.

More interestingly, the topological phase transition is more complicated in non-Abelian topological phases. For conventional topological systems characterized by Abelian charges, the transition from one topological state to another topological state involves a fixed sequential path (similar to nodes on a string or a loop as shown in Fig. S10a) and a fixed number of bandgap closing steps, and as such, the number of topological edge states is well defined. This is not the case for non-Abelian systems, where the transition from one topological phase to another one can take multiple distinct paths (like the nodes in a network as shown in Fig. S10b, which is the cycle graph of quaternion group[3]). Along different paths, the topological phase transition will close the corresponding bandgap(s), which is path-dependent. For example, from charge -1 to $+1$ there are exhaustively six distinct paths as shown in Fig. S10b. The six paths are topologically equivalent, one cannot prefer one of them just from topological viewpoint. The topological phase transitions between charges -1 and $+1$ can lead to the closing of either

the 1st bandgap or the 2nd bandgap, or even both them, depending on how we continuously tune system parameters. From this perspective we see that the topological phase transitions between charges of -1 and $+1$ are not unique, and this additional complexity implies the fickle edge states as shown in Fig. S11.

V.   Edge state evolutions in the charge -1

Although the bulk topological charge is fixed to be -1, the edge states are found to be kind of fickle (also see Ref. [1], Fig. S17). Here we first show three continuous transitions (Figs. S11a-c) in the charge -1 system and then show the corresponding edge state evolutions (Figs. S11d-f). In Fig. S11a, we rotate the rotation axis from $\hat{x}$ to $\hat{y}$ parameterized by θ_z from 0 to $\frac{\pi}{2}$. At each configuration, three eigenstates (the 1st, 2nd and 3rd bands are marked by red, green and blue, respectively) rotate 2π around the rotation axis $\hat{n} = \cos\theta_z\,\hat{x} + \sin\theta_z\,\hat{y}$. Figures S11b and c show similar transitions. In Fig. S11d, the edge states evolve with θ_z. When $\theta_z = 0$, the Hamiltonian reads,

$$
H(k) = \begin{bmatrix} 1 & 0 & 0 \\ 0 & \dfrac{1}{2}(5 - \cos 2k) & -\cos k \sin k \\ 0 & -\cos k \sin k & \dfrac{1}{2}(5 + \cos 2k) \end{bmatrix}
\tag{S8}
$$

Obviously, the first band is fully decoupled with the higher two bands in this model. Then in the PT symmetric higher two-band subspace, the edge states can be described by $\mathbb{Z}$. Here, the number of edge states is two on each edge as the two higher eigenstates rotate 2π around the x axis. Similar arguments also work at all $\theta_{x,y,z} = 0 \ or \ \frac{\pi}{2}$. However, when θ_z increases from 0, all bands start to couple with each other. Three edge states emerge and their spectral positions evolve in a complicated way (Fig. S11d).

The edge state evolution corresponds to energy pumping by simply rotating the rotation axis of eigenstates. In particular, in Fig. S11f, the pumping shows a zigzag pattern. It is also interesting to note that the energy pumping depends on non-topological properties of eigenstates, as all evolutions are occurring in the same topological phase characterized by charge -1. In the Sec. VII we try to predict some behaviours of the fickle edge states of charge -1 by going to a higher dimension (from a 2D extended plane).

VI. Non-Abelian quotient relation

We use the following three steps to prove the non-Abelian quotient relation (as schematically shown in Fig. S12).

(1) From the most general perspective, between two distinct topological phases (described by two different topological charges) there must exist bandgap closing corresponding to the topological phase transition. It works for both Abelian and non-Abelian topological phases.

(2) The topological phase transition between two distinct topological charges Q_L and Q_R is described by $\Delta Q = Q_L/Q_R$. In other words, the detail of bandgap closing is described by $\Delta Q = Q_L/Q_R$.

(3) The closing bandgap in k-space (as a bulk property) implies the domain-wall state(s) in r-space when splicing the two topologically distinct samples together (especially in the 1D system). The domain-wall state formation between charges Q_L and Q_R can be inferred from the edge state formation within the transition $\Delta Q \rightarrow +1$ (as ΔQ encodes all the topological information within the transition $Q_L \rightarrow Q_R$).

(Note that left inverse ($Q_R^{-1}Q_L$) and right inverse ($Q_L Q_R^{-1}$) show similar results finally, thus we write $\Delta Q = Q_L/Q_R$.)

Proof:

(1) The first step is obvious.

For Abelian topological phase transition, there is only one bandgap under consideration. Thus the bandgap closing happens there without any doubt.

For non-Abelian topological phase transition, there are multiple bandgaps involved. The transition requires for that there must be bandgap closing during the process. However, the position and number of bandgap closing need more details. In our three-band system, either the 1st or 2nd bandgap, or both them have to close.

$\blacksquare$

(2) The second step arises from the definition of non-Abelian topological charges (as schematically shown in Fig. S13).

Definition: The set of all homotopy classes of loops in a space X under the loop product is the fundamental homotopy group $\pi_1(X)$.

For the 1D Hamiltonian when k runs from $-\pi$ to π, the Hamiltonian traces a loop in the order-parameter space[1] $X = M_3 = \frac{O(3)}{O(1)^3}$. The quotient form of M_3 imposes that all three bands are fully gapped for any $k \in [-\pi, \pi]$. Then, each non-Abelian topological charge is well-defined via the above definition of fundamental homotopy group $\pi_1(M_3) = \mathbb{Q}$. All non-Abelian

topological charges together construct the group with satisfying all group axioms. Here, the group product is loop product between two homotopy group elements by definition. For example, the group product $\Delta Q \cdot Q_R$ indicates that k first running from $-\pi$ to π obtains charge Q_R and then k running $(-\pi \rightarrow \pi)$ again with charge ΔQ reaches to $Q_L = \Delta Q \cdot Q_R$ ($Q_{L,R}, \Delta Q \in \mathbb{Q}$). Obviously, the topological transition between charges Q_L and Q_R has to experience "k running from $-\pi$ to π with charge ΔQ". Finally, the transition between the two charges Q_L and Q_R has to make the ΔQ loop shrink to one point (basepoint), which inevitably encounters bandgap closing as long as $Q_L \neq Q_R$ ($\Delta Q \neq +1$). In other words, the bandgap closing is characterized by the charge ΔQ. Thus, the topological phase transition is described by $\Delta Q = Q_L / Q_R$.

Basically, the relation of $\Delta Q = Q_L / Q_R$ works for all of topological charges, including both Abelian and non-Abelian, for systems with single and multiple bandgaps, respectively.

$\blacksquare$

(3) We apply a 2D extended plane and Jackiw-Rebbi argument to finish the third step.

First we extend the 1D Hamiltonian $H(k)$ (Eq. 2 or Eq. S6) onto a 2D extended plane,

$$H(k) = \bar{H}(\cos k, \sin k) \rightarrow \tilde{H}(k_1, k_2) \tag{S9}$$

where we applied the substitution $\cos k \rightarrow \rho \cos k = k_1 \; and \; \sin k \rightarrow \rho \sin k = k_2$ with $\rho \in [0,1]$. It is worth noting that the substitution preserves PT symmetry with $\tilde{H}(k_1, k_2) = \tilde{H}^*(k_1, k_2)$. The parameter ρ can be absorbed by those hopping parameters in Eq. 1 (or Eq. S5) in actual implementation.

Figure S14a shows the 2D band structure for charge $+i$, where the original Hamiltonian $H(k)$ exactly locates on the unit circle $k_1^2 + k_2^2 = 1$ (black solid circle). According to the definition of non-Abelian topological charges, there must be band degeneracy for those non-trivial topological charges ($\neq +1$), i.e., Dirac cone, in the range $k_1^2 + k_2^2 < 1$ as one can see in Fig. S14a. They cannot be removed unless topological phase transition happens with the degeneracy point moving out of the unit circle.

Then we apply the Jackiw-Rebbi type argument[4] to show that there must be domain-wall state relating to the topological phase transition. In Fig. S14a-c, we take the $+i$ charge as an example. First, by the tuning system parameters, we continuously shrink the unit circle (black circle in Fig. S14a) into the magenta one, which still belongs to the charge $+i$ as long as the Dirac point lies within the circle. Secondly, when we further shrink the magenta circle as shown in Fig. S14b, topological phase transition happens and the 2nd bandgap closes as the Dirac point sits on the magenta circle. Finally, the degeneracy point of Dirac cone stands outside the magenta circle and the topological charge becomes $+1$ (Fig. S14c). Figures S14d-f give the corresponding 1D band structures along the polar angles of the three magenta circles. In the vicinity of the transition point $\theta = \pi$, the PT-symmetric Hamiltonian can be parameterized as $H = \delta k_\theta \sigma_x - \delta m \sigma_z$ (Fig. S14d) and $H = \delta k_\theta \sigma_x + \delta m \sigma_z$ (Fig. S14f) with $0 < \delta m \ll 1$ being the mass term. The standard Jackiw-Rebbi argument states that there must be one domain-wall state between them two, described by $H = -i\partial_x \sigma_x + m(x)\sigma_z$ and $\lim_{x \to \pm\infty} m(x) = \pm 1$. When one considers the Dirac cone between the 1st and 3rd bands, the edge states in charge $+j$ (Fig. S15b) can be explained similarly. The arguments also work for the quadratic degeneracy as shown in Fig. S15e with charge -1. The difference for the charge -1 is that the degeneracy is quadratic, which can split into to two linear Dirac cones upon small perturbation and hence it carries two edge states (per edge).

From the above arguments, we see that the bandgap that the edge states locate in is implied by the position of degeneracy in the 2D extended space. Finally, the number of extended 2D band degeneracies (as given by the number of linear Dirac cones) is equal to the number of edge states per edge. We conclude that the topological phase transition in k-space (bulk) implies the presence of topological edge/domain-wall states in r-space. More specifically, where there is a bandgap closing there is an edge/domain-wall state.

Therefore, the edge/domain-wall states are characterized by $\Delta Q = Q_L/Q_R$ as it fully describes the topological phase transition (from Step 2).

$$\blacksquare$$

VII.   Predict edge states from the extended 2D plane

In the following we show some examples (Figs. S15-S19) to illustrate the above arguments. Fig. S15 shows the flat-band cases. For charge $+i$ (Fig. S15a), there is one Dirac cone between the 2nd and 3rd bands, thus the 2nd bandgap supports one edge state per edge (see Fig. 2b in the main text). In the flat band model, the 2nd band is fully decoupled for the charge $+j$ (Fig. S15b) and thus the Dirac cone is constructed between the 1st and 3rd bands. There is one edge state (per edge) merging in the 2nd band (BICs in Fig. 2c in the main text). For charge -1 (Fig. S15e) there is a quadratic band degeneracy between the 1st and 2nd bands, which can split into two linear Dirac cones upon small perturbation. Thus, there are two edge states per edge (see Fig. 2e in the main text) in the 1st bandgap. Figure S15d gives the trivial case with charge $+1$, there is no degeneracy in the unit circle as expected, and thus there is no topological edge state.

Figure S16 shows the 2D extended band structures for our experiment systems. They share very similar arguments with Fig. S15. Except that both charges $+j$ and -1 exhibit triple linear degeneracies and support one edge state per bandgap (per edge) (see Figs. S5b and d), it is due to that the linear triple degeneracy may split into two linear Dirac cones as well. Here, the 2nd band in both cases are not decoupled. Therefore, the edge states of charge $+j$ are different from the decoupled case as shown in Fig. S15b (see details in Sec. III and Fig. S6).

Figure S17a (see Fig. S11a for the definition of θ_z) shows the case of charge -1, we argue that the two edge states in the upper bandgap are of topological origin, while the edge state in the lower bandgap is non-topological in the 1D system. The appearance of latter is mainly due to the introduction of the new parameter θ_z, which effectively pumps the lowest edge state across the 1st bandgap. However, at a given value of θ_z, we argue that the lowest edge state is trivial as it can be removed by continuously tuning $\theta_z \to 0$ (i.e. parameter changing without bandgap closing). It is possible to give a topological meaning to the existence of the lowest edge state if one considers θ_z as a synthetic dimension, so that the whole system is promoted to one-dimension higher (i.e. a 2D system). It is worth noting that the synthetic 2D space of (k, θ_z) is different from our previous extended plane spanned by (k_1, k_2) in Sec. VI, the latter is introduced to show the topological reason of each 1D non-Abelian topological phase and further predict the positions of edge states. Here, pumping edge state via parameter θ_z is similar to Thouless pump – integer charge is pumped across a 1D insulator in one period of an adiabatic cycle, which has been widely employed to understand the edge states of Chern insulator[5,6].

Therefore, here we only focus on the edge states in the upper bandgap. During this evolution from $\theta_z = 0 \to \frac{\pi}{2}$, the two edge states (per edge) hosted by the 2nd bandgap gradually merge

into the 2nd band. This can be understood from the evolution of the extended 2D Hamiltonian in the extended 2D plane, as shown in Figs. S17b-f. Initially there is a quadratic degeneracy at the origin inside the unit circle between the 2nd and 3rd bands, ensuring the presence of two edge states in the upper bandgap. Gradually, the quadratic degeneracy point of the two higher bands is lowered as system parameter changes (with keeping quadratically touched), and eventually forms a triple degeneracy with the lowest band. Meanwhile the 2nd band becomes flat and it decouples from the 1st and 3rd bands. Thus, two edge states (per edge) are guaranteed to merge into the 2nd band. Note that during this process, there is no band crossing along the unit circle, ensuring that there is no topological transition in the original 1D Hamiltonian $H(k)$. We further show the gradual transition of $\theta_x = 0 \rightarrow \frac{\pi}{2}$ in Fig. S18, which shows similar features as those in Fig. S17, except for that the quadratic degeneracy is between the two lower bands.

For the gradual transition ($\theta_y = 0 \rightarrow \frac{\pi}{2}$) shown in Fig. S19, the three edge states in the two bandgaps form a 'z' pattern. It shows that between the two bands that have quadratic degeneracy in the 2D extended plane (the lower two bands in Figs. S19b-c, and the higher two bands in Figs. S19e-f), there are always two edge states (per edge) located in the bandgap of the corresponding 1D system. Interestingly, at the transition point ($\theta_y = \frac{\pi}{4}$) where the quadratic degeneracy is transferred from the two lower bands to the two higher bands, a linear triple degeneracy is formed between the three bands (Fig. S19d), which resembles the band structure of charge $+j$ as shown in Fig. S15b. However, one should note that in contrast to the case of $+j$, in which the 2nd flat band is decoupled from other two bands, while here all three bands have to be coupled together to realize the linear triple degeneracy in Fig. S19d for charge -1. In other words, the decoupled triple degeneracy of charge -1 must be quadratic as shown in Fig. S17f (Fig. S18b).

In Fig. S20, we have summarized all different types of the extended 2D band degeneracies in Figs. S15-S19. By fixing the six black dots on the two sides in each panel, the degenerate points may vary between Figs. S20b to c for charges $+j$ and between Figs. S20e-h for charge -1. Following our main argument in Sec. VI, "where there is a bandgap closing there is an edge/domain-wall state", we conclude that: 1. For the bandgap supporting linear/quadratic double degeneracy, there must exist one/two edge states (per edge) in the corresponding bandgap; 2. For the coupled linear triple degeneracy, there is one edge state per bandgap (per edge), i.e., for both the 1st and 2nd bandgaps, each supports one edge state per edge; 3. Special cases with decoupled triple degeneracy can be regarded as two-band systems, one/two edge states may merge into the 2nd band for linear/quadratic triple degeneracy in the form of BICs. Therefore, with providing the degeneracy information in the extended 2D plane one can predict the topological edge states, especially for charge -1.

The edge states of hard boundaries can be regarded as the domain-wall states between various non-Abelian topological charges and $+1$. For the domain-wall states between two arbitrary non-Abelian topological charges, one can combine the above arguments and the non-Abelian quotient relation of $\Delta Q = Q_L / Q_R$ together to make similar predictions.

Coincidentally, in our experiment due to the special onsite energy setting, i.e., $S_{AA} = S_{BB}$ in Tab. S2, both j and -1 cases happen to be linear triple degenerate as shown in Figs. S16b and d.

VIII.   Domain-wall states

The parameters used to construct the domain-walls in Fig. 4 (main text) are listed in Tab. S3. Figure S21 shows the corresponding domain-wall (dashed box) settings, where points and lines indicate the onsite energies and NN hoppings, respectively. Worth mentioning on the domain-wall is that its onsite energies may sensitively contribute to the trivial domain-wall states. In addition, we neglect those edge states localized on the two hard boundaries when studying the domain-wall states in both the simulation and experiment.

The arrows/triangles indicate the excitation/probing positions in the experiment measurements. In the charge pair $(+i, -i)$, two excitation/probing positions are used to fully excite/measure the domain-wall states. This is due to the special spatial distributions of the domain-wall states as shown in Fig. S22. For two of three domain-wall states (the 1st and 3rd in Fig. S22b), we need to probe them at the unit cell indicated by the orange triangle, while the last (the 2nd in Fig. S22b) one can only be probed at the position of gray triangle.

Table S3. Coefficients of tight binding models used for the domain-wall state measurements.

Q	s_{AA}	s_{BB}	s_{CC}	v_{AA}	v_{BB}	v_{CC}	u	v	w
$+i$	2	2	-4	-1	1	0	-1	-1	0
$+j$	0	0	0	-2	2	0	-1	1	0
$+k$	-2	-2	4	-1	1	0	-1	-1	0
$-i$	2	2	-4	-1	1	0	1	1	0
-1	0	0	0	-2	0	2	-2	1	0

IX. Method: Transmission line theory and experimental characterization

Transmission line theory

In order to observe the non-Abelian topological charges experimentally, we implement the tight binding model using transmission line networks with braiding connectivity. For a network connected by transmission lines, the wave function of each node satisfies the network equation[7-9]:

$$-\psi_m \sum_n \left[\sum_{k=1}^{N_{mn}} \coth\left(z l_{mn}^{(k)}\right) \right] + \sum_n \left[\sum_{k=1}^{N_{mn}} \frac{1}{\sinh\left(z l_{mn}^{(k)}\right)} \right] \psi_n = 0 \tag{S10}$$

where ψ_m and ψ_n are, respectively, wave amplitudes at nodes m and n, N_{mn} denotes the cable number connecting nodes m and n, $l_{mn}^{(k)}$ is the length of the *kth* cable between nodes m and n, $z = (i\omega/c_0)\sqrt{\epsilon_r}$ with ω, c_0 and ϵ_r being the angular frequency, the speed of light in vacuum, and the relative permittivity of the dielectric medium in the coaxial cables, respectively. In the lossless case, z is a purely imaginary number. If we set all the lengths of cables to be the same $l_{mn}^{(k)} = l_0$ and each node connects the same number of cables N_0, the Eq. (S10) can be deformed to:

$$\sum_n N_{mn} \psi_n = N_0 \cos(g l_0) \cdot \psi_m \tag{S11}$$

where $g = (\omega/c_0)\sqrt{\epsilon_r}$ is a purely real number for lossless case. This equation form is mathematically equivalent to the tight binding equation with eigen-energy $N_0 \cos(g l_0)$ and hopping strength N_{mn} between nodes m and n. The on-site energy can also be realized by connecting cables staring from node m and ending also at node m itself to form loops, then on-site energy is $N_{mm} = 2j$, where j is the number of loops on node m. Thus, transmission line network offers an ideal platform to realize various tight binding models.

To show how to relate the transmission line network with tight binding model, we take a 1D periodic system as an example as shown in Fig. S23.

In the pedagogical example, we just assume there are two sublattices A and B in one unit-cell connected by N_1 transmission lines and they are also connected with the sublattices of the neighbouring unit cells by N_2 transmission lines. All the transmission lines have the same length l_0 and the lattice constant is a. According to the transmission line equation, we can write the following equation for node A:

$$-(N_1 + N_2) \cdot \cot(gl_0) \cdot \psi_A + \left[\frac{N_1}{\sin(gl_0)} + \frac{N_2}{\sin(gl_0)} \cdot \exp(-ik_x a)\right] \cdot \psi_B = 0 \quad \text{(S12)}$$

The k_x is the Bloch wave vector. For node B, we can also write its equation in the same way:

$$\left[\frac{N_1}{\sin(gl_0)} + \frac{N_2}{\sin(gl_0)} \cdot \exp(ik_x a)\right] \cdot \psi_A - (N_1 + N_2) \cdot \cot(gl_0) \cdot \psi_B = 0 \quad \text{(S13)}$$

By combining the Eqs. S12 and S13 and after some deformation, we can get the matrix form of the transmission line equations:

$$\begin{bmatrix} 0 & N_1 + N_2 \cdot \exp(-ik_x a) \\ N_1 + N_2 \cdot \exp(ik_x a) & 0 \end{bmatrix} \begin{bmatrix} \psi_A \\ \psi_B \end{bmatrix} = (N_1 + N_2)\cos(gl_0) \begin{bmatrix} \psi_A \\ \psi_B \end{bmatrix} \quad \text{(S14)}$$

We see that Eq. S14 is an eigen-equation of the tight binding model with eigen-energy of $(N_1 + N_2)\cos(gl_0)$. The intra-unit cell hopping term is N_1 and the inter-unit cell one is N_2. This example shows that the transmission line network can exactly mimic a tight binding model with integer hoppings.

Figure S24 shows the realistic connectivity in transmission line networks towards realizing the cases shown in Fig. 3 in the main text.

Experimental characterization

The tight-biding model in the main text (Eq. 2) looks deceptively simple but its experimental realization is a bit tricky as it requires complex number hoppings. To realize the complex hoppings, the network is required to have multiple nodes in each meta-atom[10]. Each meta-atom is actually the compactification of a hidden dimension carrying four nodes (layers) from top to down as shown in the inset of Fig. 3a. We label the four nodes in one meta-atom by indices *1, 2, 3 and 4* from top to bottom. As such, there are four allowed subspaces. Each subspace can be characterized by a pseudo angular momentum with $e^{i4\varphi_n} = 1$ ($n = 1,2,3,4$), with $\varphi_1 = 0, \varphi_2 = \frac{\pi}{2}, \varphi_3 = \pi \ and \ \varphi_4 = -\frac{\pi}{2}$. We work with the subspace $\varphi_2 = \frac{\pi}{2}$ to realize our 3×3 Hamiltonian and within this subspace, the eigenfunctions in the 4 nodes have relative phases of $(1, i, -1, -i)$. When we specifically excite the four-nodes inside the meta-atom with a relative constant phase shift $\frac{\pi}{2}$ as $(1, i, -1, -i)$, in the subspace the time-reversal symmetry is effectively broken, following the same way as that each spin space (if applicable) in the Kane-Mele model breaks the time-reversal symmetry. Of course, there exists its time-reversal counterpart subspace $(1, -i, -1, i)$, but there is no conversion between them (i.e. the system contains two block-diagonalized time-reversal counterparts, in a similar way as the Kane-Mele model).

When we excite one meta-atom by imposing the phase shift, the excitation only has projection on the eigenmodes of the selected sub-space (and is orthogonal to the modes in other sub-spaces) and hence only the three modes in that subspace are excited. In other words, each subspace corresponds to a pseudo angular momentum (as mentioned in the main text), and as long as the angular momentum is preserved, other subspaces are not excited. In the experiment, we checked the results by making the projection of the measured data onto the specified

subspace and we indeed found that the projection is nearly 100%, reassuring that the leakage into other subspaces (due to imperfections) is negligibly small.

There are three meta-atoms in a unit cell labelled with A, B, and C. In total, 12 nodes are constructed in each unit cell. As mentioned above, the whole system can be block-diagonalized into the four disjoint subspaces represented by the four pseudo angular momenta, and each subspace contains three degrees of freedom. Here we only consider one subspace, which corresponds to three bands, the rest of $12 - 3 = 9$ bands goes beyond our interests here.

In experiment, we use a signal generator (Keysight 8647A Synthesized Signal Generator) which is marked with 'S' as shown in Fig. S25 to be the source, and an oscilloscope marked with 'O' (Keysight DSOX2002A Oscilloscope) to measure the voltage at each meta-atom. The AC frequency signal from the signal generator is input to the nodes of one meta-atom by cable 1 as indicated with the red arrow. The eigenmodes in the topological networks are excited by the input signal, all meta-atoms together provide the corresponding voltage distributions. To measure the voltage at each node without breaking the original system, we directly connect the node to the oscilloscope using a short cable (cable 2). The impedance of the oscilloscope is much higher compared to the transmission lines ($1M\Omega\ to\ 50\ \Omega$), so the oscilloscope connected to the node with very short line could be regarded as a hard wall to our system. The influence of the measurement equipment to our system could be ignored in this way.

Here cable 3 is used to provide a reference signal for the phase measurement. To excite the specified eigenmodes better, the AC signals are input to the four-layer nodes with a phase shift $\frac{\pi}{2}$ of meta-atoms A, B and C successively in a designated unit cell. With each excitation, both

the amplitude and phase of the site-resolved voltage from all the meta-atoms in our transmission line networks are recorded. The Bloch wave functions can be obtained after Fourier transformation, which give the experimental band structures and eigenstate mappings of our system.

We measured the bulk spectrum using an open chain containing 13 unit cells (and about 470 coaxial cables). In our measurement of bulk bands, the signal is injected from the middle position of the open chain that is very far away from the boundary so that the edge states cannot be excited. For the detection of edge/domain-wall states, the signal is injected at the positions near the edge/domain-wall.

In realistic systems, eigenvectors are not gauge invariant, it is hard to measure without imposing some extra conditions. In other words, one has to fix the gauge field first and then map them in the experiment. First we design the PT symmetric Hamiltonian (Eq. 2) to be real (via carefully introducing complex hoppings). Consequently, the eigenvectors are real as well. From this perspective, the only freedoms left are $\pm|u_X(k)\rangle$ $with$ $X = A, B, C$. Finally, we impose the right-handed rule to the eigenstate frame, i.e., $(|u_A(k)\rangle \times |u_B(k)\rangle) \cdot |u_C(k)\rangle > 0$, when plotting the eigenstate frame sphere.

X.   Reference

1   Wu, Q., Soluyanov, A. A. & Bzdušek, T. Non-Abelian band topology in noninteracting metals. *Science* **365**, 1273 (2019).

2   Mermin, N. D. The topological theory of defects in ordered media. *Rev. Mod. Phys.* **51**, 591-648 (1979).

3   Shanks, D. *Solved and Unsolved Problems in Number Theory*. 2nd edn, pp. 85 (Chelsea, New York, 1978).

4   Jackiw, R. & Rebbi, C. Solitons with fermion number 1/2. *Phys. Rev. D* **13**, 3398-3409 (1976).

5   Xiao, D., Chang, M.-C. & Niu, Q. Berry phase effects on electronic properties. *Rev. Mod. Phys.* **82**, 1959-2007 (2010).

6   Ozawa, T. et al. Topological photonics. *Rev. Mod. Phys.* **91**, 015006 (2019).

7   Zhang, Z. Q. et al. Observation of localized electromagnetic waves in three-dimensional networks of waveguides. *Phys. Rev. Lett.* **81**, 5540-5543 (1998).

8   Zhang, Z.-Q. & Sheng, P. Wave localization in random networks. *Phys. Rev. B* **49**, 83-89 (1994).

9   Jiang, T. et al. Experimental demonstration of angular momentum-dependent topological transport using a transmission line network. *Nat. Commun.* **10**, 434 (2019).

10   Zhao, E. Topological circuits of inductors and capacitors. *Ann. Phys. (N. Y.)* **399**, 289-313 (2018).

11   Wikipedia contributors. "Quaternion group", Wikipedia, The Free Encyclopedia, https://en.wikipedia.org/w/index.php?title=Quaternion_group&oldid=1001235481 (2021).

XI. Figures
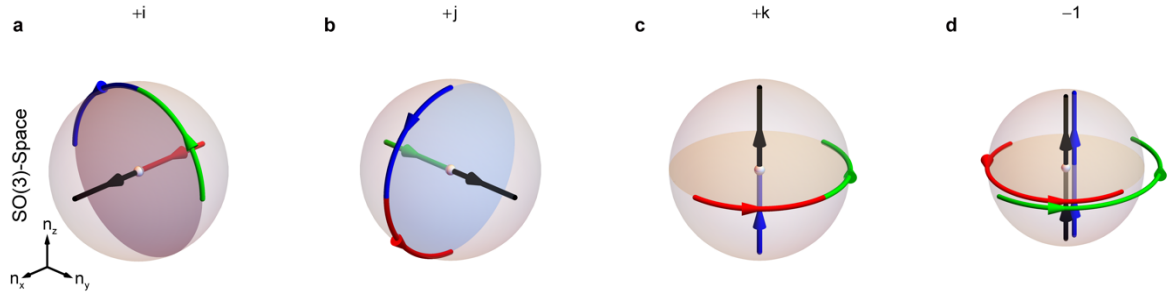
Figure S1 | a-d The curve cosets of D_2 in $SO(3)$ space corresponding to Figs. 1b-e in the main text, respectively. Black, red, green and blue curves indicate $R(k)$ acting on $D_2 = [I, R(\hat{x}, \pi), R(\hat{y}, \pi), R(\hat{z}, \pi)]$, respectively. One can form the topological space X/H with identifying points of X which can be related by some element of H ($x \equiv xh$). This is to intuitively show the fundamental homotopy group of space $\frac{SO(3)}{D_2}$.
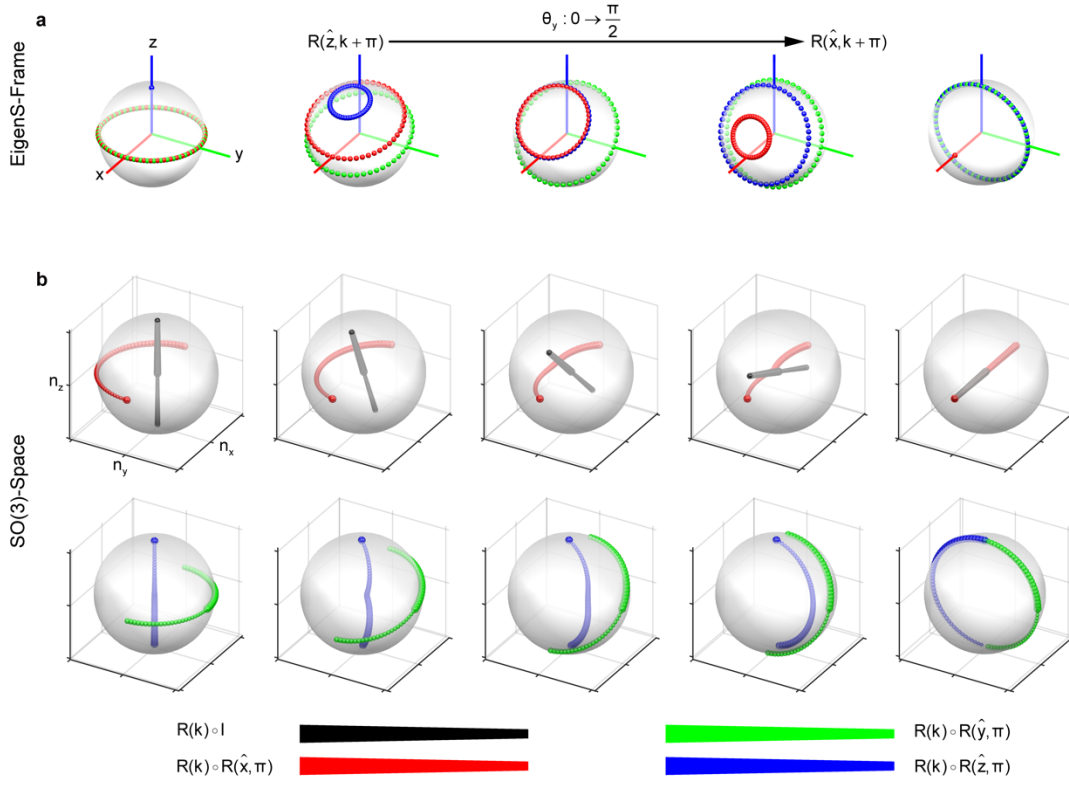
Figure S2 | Continuous transition of charge -1 in SO(3) space. a, Eigenstate frames vary along with the rotation of rotation axis. The rotation axis is defined as $\hat{n} = \cos\theta_y\,\hat{z} + \sin\theta_y\,\hat{x}$. Red/green/blue indicates the eigenstate trajectory of the 1st /2nd /3rd band. **b,** The corresponding curve cosets of D_2 in $SO(3)$ space. Black, red, green and blue curves indicate $R(k)$ acting on $D_2 = [I, R(\hat{x},\pi), R(\hat{y},\pi), R(\hat{z},\pi)]$, respectively. Here, $SO(3)$ space is a solid sphere embedded in the three-dimensional space $\mathbb{R}^3$ with a radius of π. Each point is parametrised by the rotation with normalized axis $\hat{n}(k)$ and rotation angle $\phi(k)$ as $R[\hat{n}(k), \phi(k)] = \exp[\phi(k)\,\hat{n}(k)\cdot\vec{L}]$. The wedge colorbars indicate the direction of wavevector k running from $-\pi$ to $+\pi$.
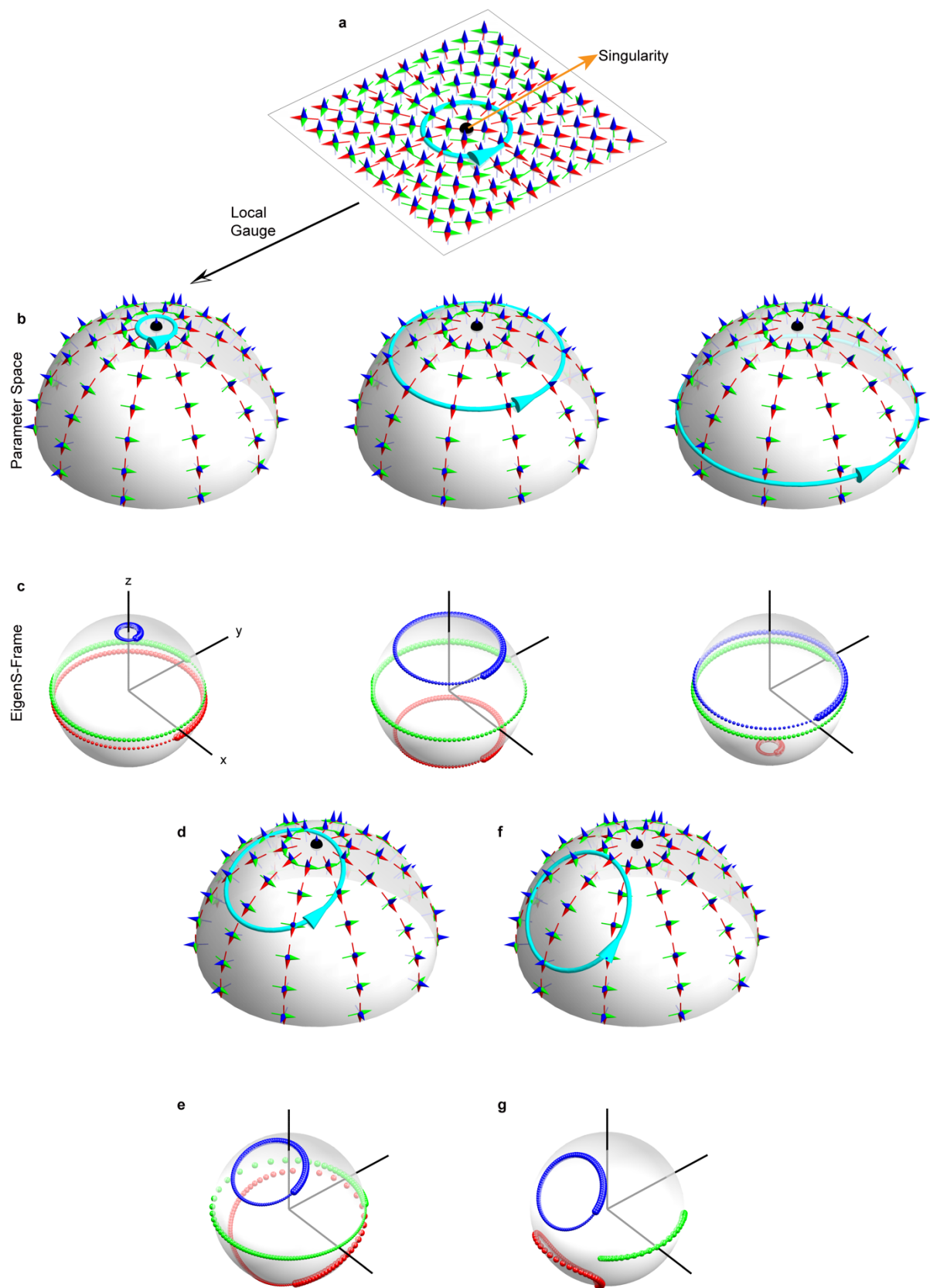
Figure S3 | Continuous transition in the charge -1. a, Triad-vector field with a singularity located at the centre. **b,** Mapping the triad-vector field on to a semi-sphere. **c,** Eigenstate trajectories ($k: -\pi \to \pi$) along the cyan loops shown in (b). Red/green/blue indicates the eigenstate trajectory of the 1st /2nd /3rd band. **d,** Tilted cyan loop encircling the singularity. **e,** The trajectories of three eigenstates corresponding to (d). **f,** Contractible cyan loop without encircling the singularity indicating charge $+1$. **g,** The trajectories of three eigenstates corresponding to (f) are contractible. The arrow position indicates the start point in (a, b, d and f), corresponding to the thickest point in (c, e and g).
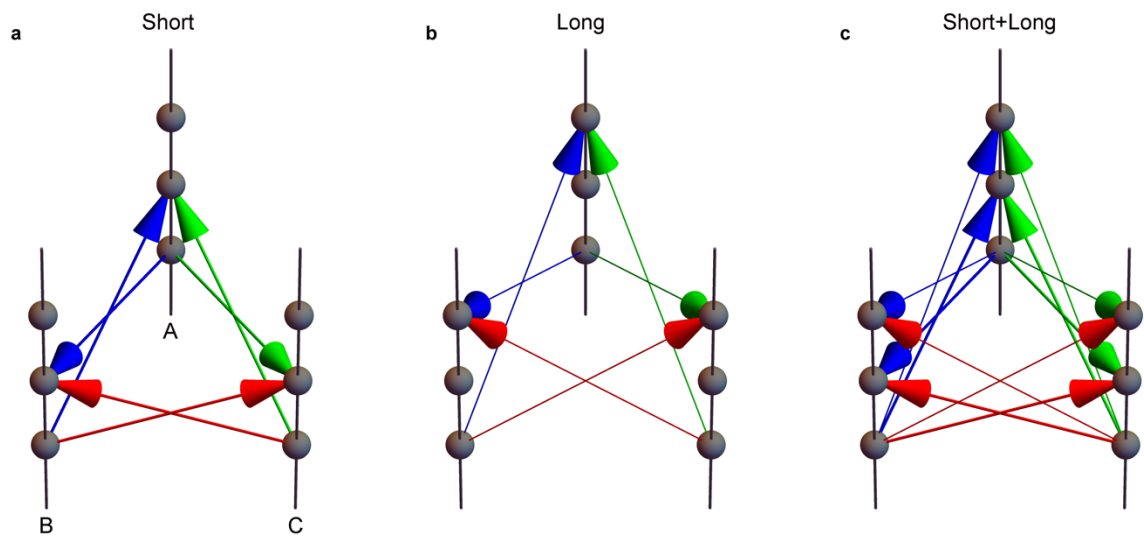
Figure S4 | Tight binding ladder with three legs. a, 'Short' indicates the NN (nearest neighbour) hoppings. **b,** 'Long' indicates the NNN (next nearest neighbour) hoppings. **c,** The case when considering both the NN and NNN hoppings together. For brevity, $s_{XY}c^{\dagger}_{X,n}c_{Y,n}(X,Y=A,B,C \text{ and } X \neq Y)$ hoppings are not illustrated.
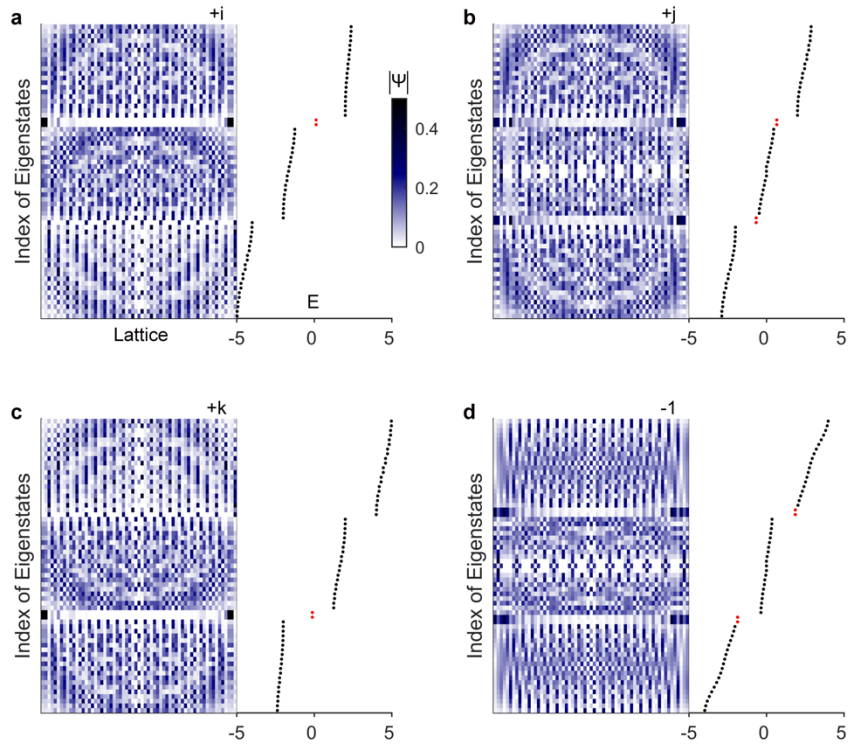
Figure S5 | Edge states at hard boundaries with parameters listed in Tab. S2. a-d, Edge states (red dots) at hard boundaries for charges $+i$, $+j$, $+k$ and -1, respectively. The eigenstate distributions (left panels) are illustrated accompanying with the eigen-energy profiles (right panels).
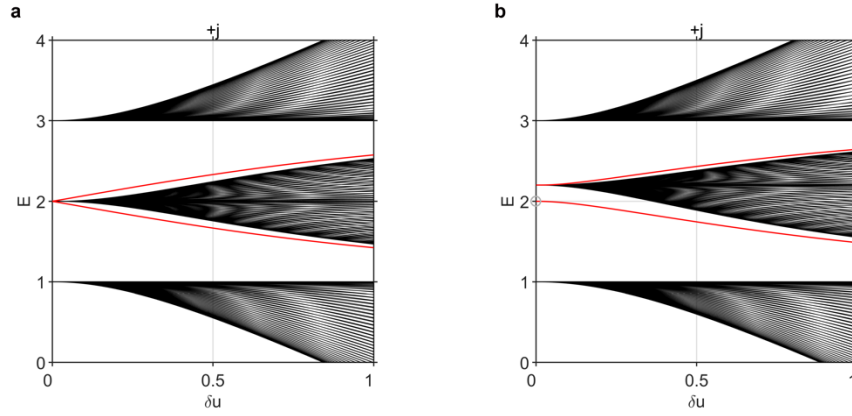
Figure S6 | Coupling of the 2nd band induces one more edge state (red line) per edge in the charge +*j*. a and b, Corresponding to $s_{BB} = 2$ and $s_{BB} = 2.2$, respectively. When $\delta u = 0$, the 2nd band is decoupled from the other two bands, the system can be regarded as a two-band system. There is only one edge state per edge as indicated by the gray circle in (b) (see Fig. 2c in the main text corresponding to (a)), while one more edge state (per edge) emerges from the middle (2nd) band when $\delta u > 0$ (switching on the coupling). (Parameter setting, $u \rightarrow u + \delta u$, the rest is from Tab. S1)
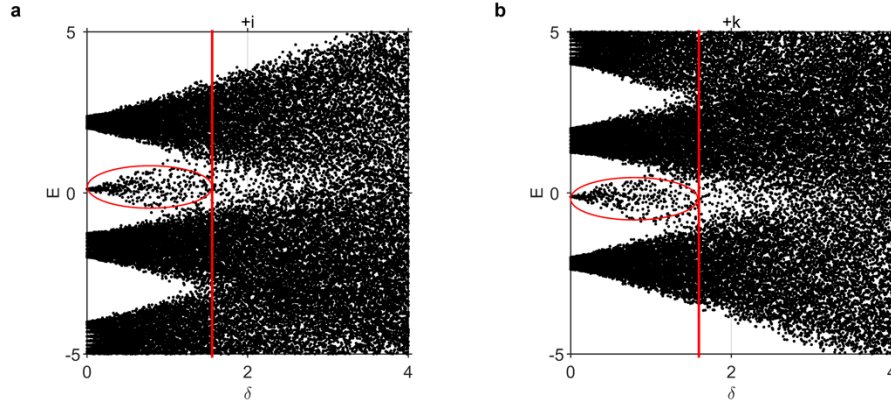
Figure S7 | Robustness of edge states against disorder for charges $+i$ (a) and $+k$ (b). The solid red lines indicate non-Abelian topological phase transitions (as long as one of two bandgaps is closed) with increasing the disorder strength δ added onto s_{AA}, s_{BB} *and* s_{CC}, i.e., $s_{AA,n} = s_{AA} + \epsilon_A(|\epsilon_A| < \delta)$ with n indicating the site number (Parameters are from Tab. S2). The red ellipses indicate the corresponding edge states.
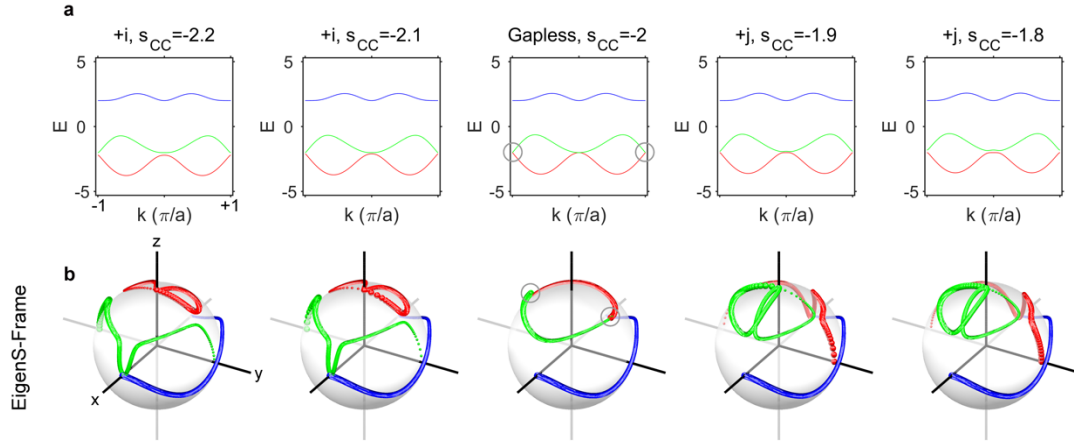
Figure S8 | Topological phase transition from charge $+i$ to $+j$. a, Band structure transition experiencing bandgap opened→closed→reopened process. The gray circles indicate linear band crossings. The quadratic degeneracy at $k = 0$ is accidental. **b,** The corresponding eigenstate frame transition. The gray circles indicate the double degeneracies of eigenstates at $k = \pm\pi$. Red/green/blue colour indicates the eigenstate trajectory of the 1st /2nd /3rd band. The direction of line-width decreasing indicates $k: -\pi \to \pi$. The rest parameters are $v_{AA} = -1, v_{BB} = 1, u = -1, v = 1$.
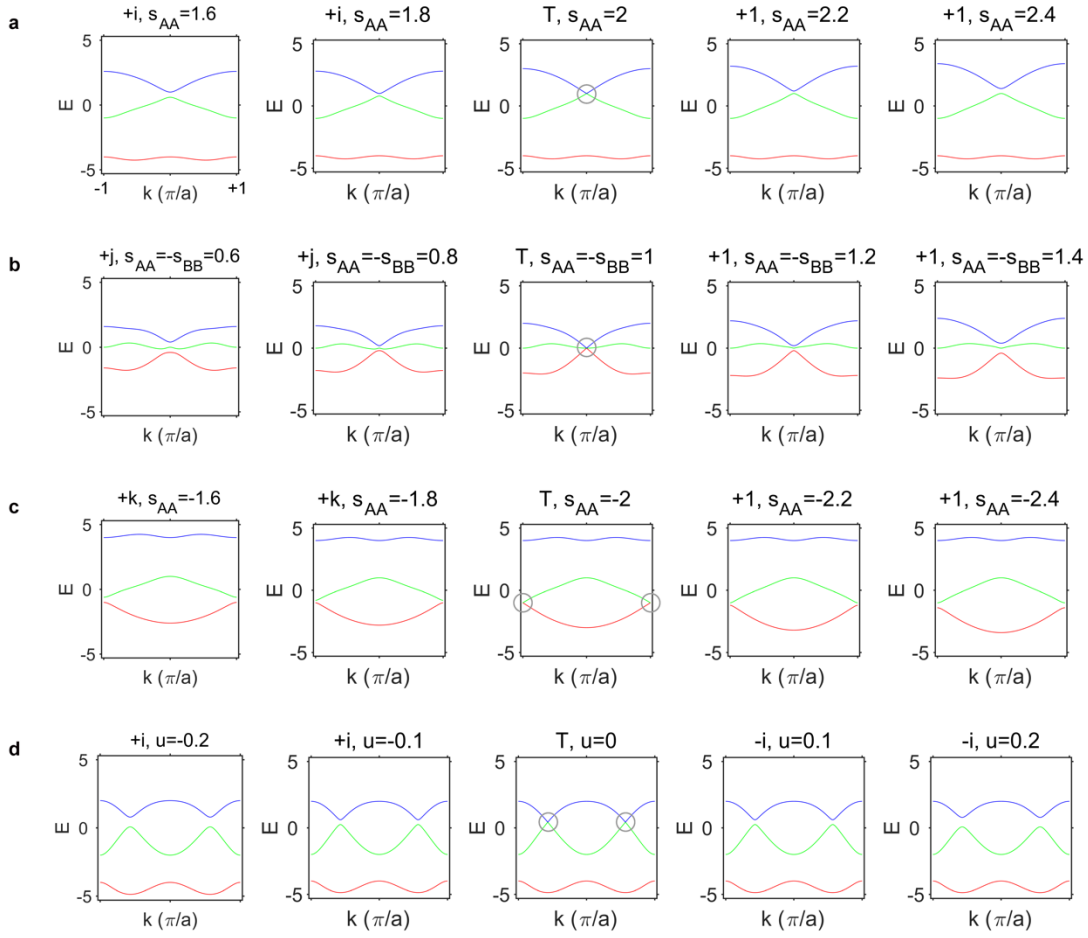
Figure S9 | Topological phase transition (T) from charges $+i$ to 1 (a), $+j$ to 1 (b), $+k$ to 1 (c) and $+i$ to $-i$ (d). Two linear crossings in (d) arise during the transition implies a change of charge $\Delta Q = i/-i = -1$. All others experience only one linear crossing. (Parameter setting, a: $s_{CC} = -4, v_{AA} = -\frac{1}{2}, v_{BB} = \frac{1}{2}, u = -\frac{1}{2}, v = \frac{1}{2}$; b: $v_{AA} = -\frac{1}{2}, v_{BB} = \frac{1}{2}, u = -\frac{1}{2}, v = \frac{1}{2}$; c: $s_{CC} = 4, v_{AA} = -\frac{1}{2}, v_{BB} = \frac{1}{2}, u = -\frac{1}{2}, v = \frac{1}{2}$; d: $s_{CC} = -4, v_{AA} = -1, v_{BB} = 1, v = 1$; the rest are all 0)
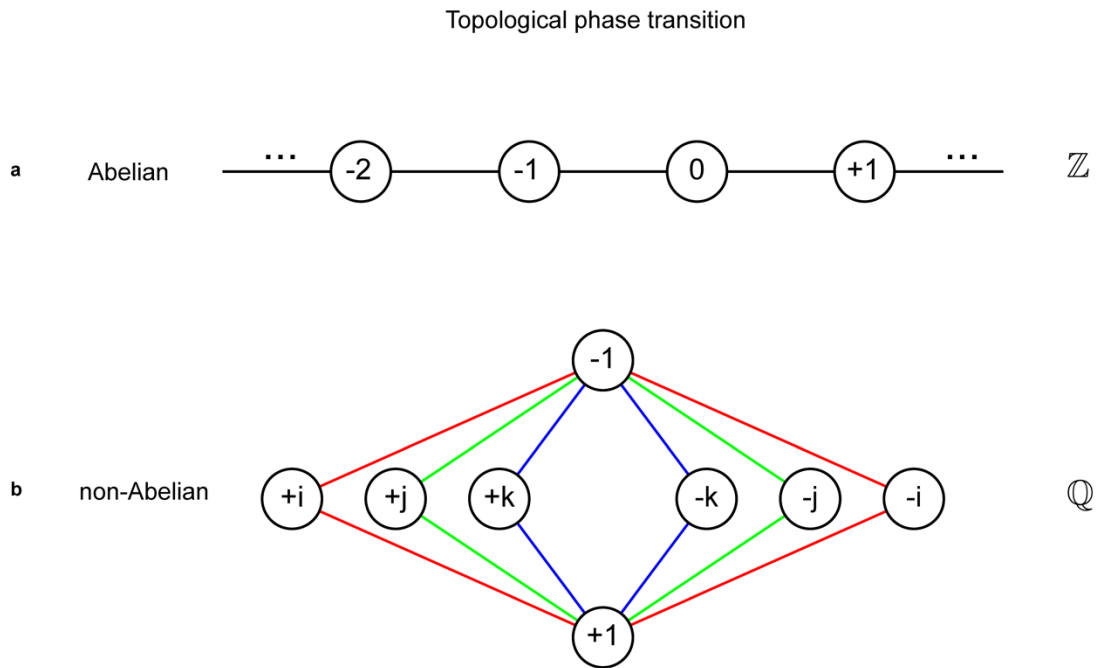
Figure S10 | Topological phase transition with Abelian (a) and non-Abelian (b) topological charges. b, (ref. [11]) Cycle graph of the quaternion group $\mathbb{Q}$. In the Abelian topological phase, the topological phase transition is single pathed. While in the non-Abelian topological phase, the topological phase transition is multiple-pathed. There are six paths that the system can be changed from charge -1 to $+1$, and the bandgap closing details are different in these paths.
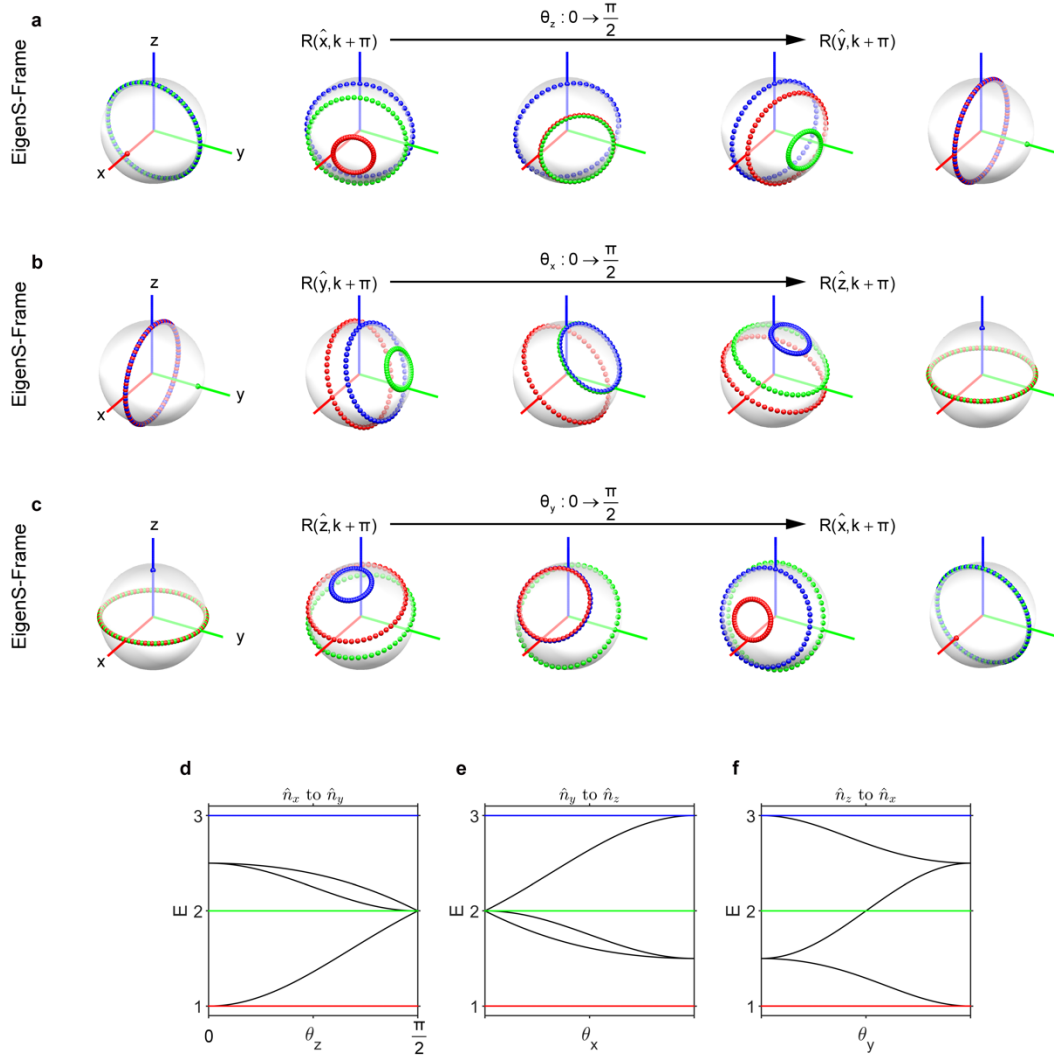
Figure S11 | Continuous transition parametrized by $\theta_{x,y,z}$ in the charge -1. a, The eigenstate frame evolving with rotating the rotation axis $\hat{x}$ to $\hat{y}$ as parametrized by $\theta_z: 0 \to \frac{\pi}{2}$. The rotation axis is defined as $\hat{n} = \cos\theta_z\,\hat{x} + \sin\theta_z\,\hat{y}$. **b,** Similar to (a) but for $\hat{y} \to \hat{z}$. The rotation axis is defined as $\hat{n} = \cos\theta_x\,\hat{y} + \sin\theta_x\,\hat{z}$. **c,** Similar to (a) but for $\hat{z} \to \hat{x}$. The rotation axis is defined as $\hat{n} = \cos\theta_y\,\hat{z} + \sin\theta_y\,\hat{x}$. Red/green/blue color indicates the eigenstate trajectory of the 1st /2nd /3rd band. **d/e/f,** Edge states (black lines) evolve with $\theta_{z/x/y}$ defined in (a/b/c). The 1st, 2nd and 3rd bulk bands are coloured in red, green and blue, respectively.
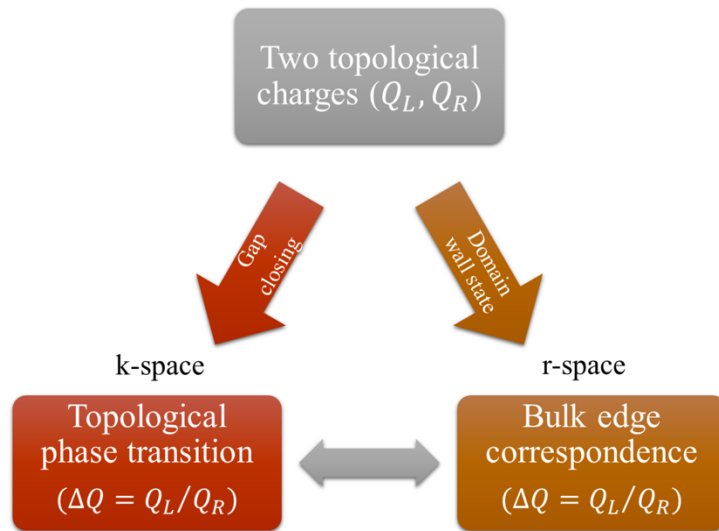
Figure S12 | Flow chart for proving the non-Abelian quotient relation.
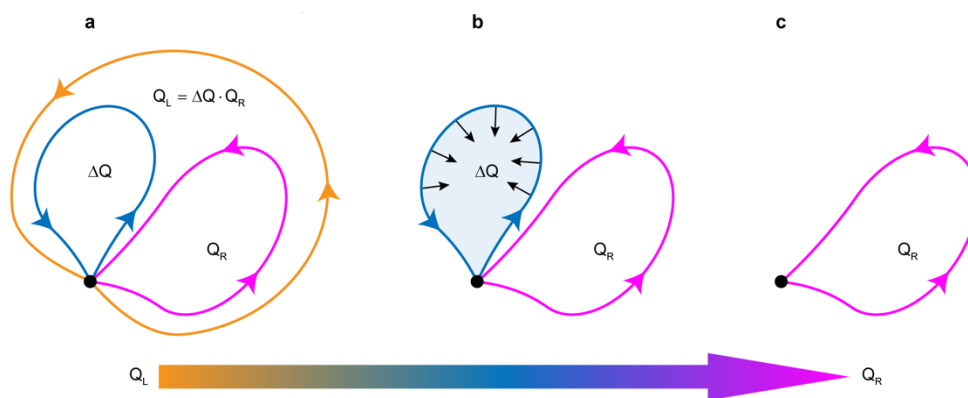
Figure S13 | The loop product in the fundamental homotopy group and topological phase transition from Q_L (a) to Q_R (c) with shrinking the blue loop ΔQ (b) to the basepoint (black dot). a, The charge $Q_L = \Delta Q \cdot Q_R$ indicated by the loop product. **b,** Shrinking the charge ΔQ loop to be the basepoint to enable the topological phase transition from Q_L to Q_R. **c,** The charge Q_R after topological phase transition.
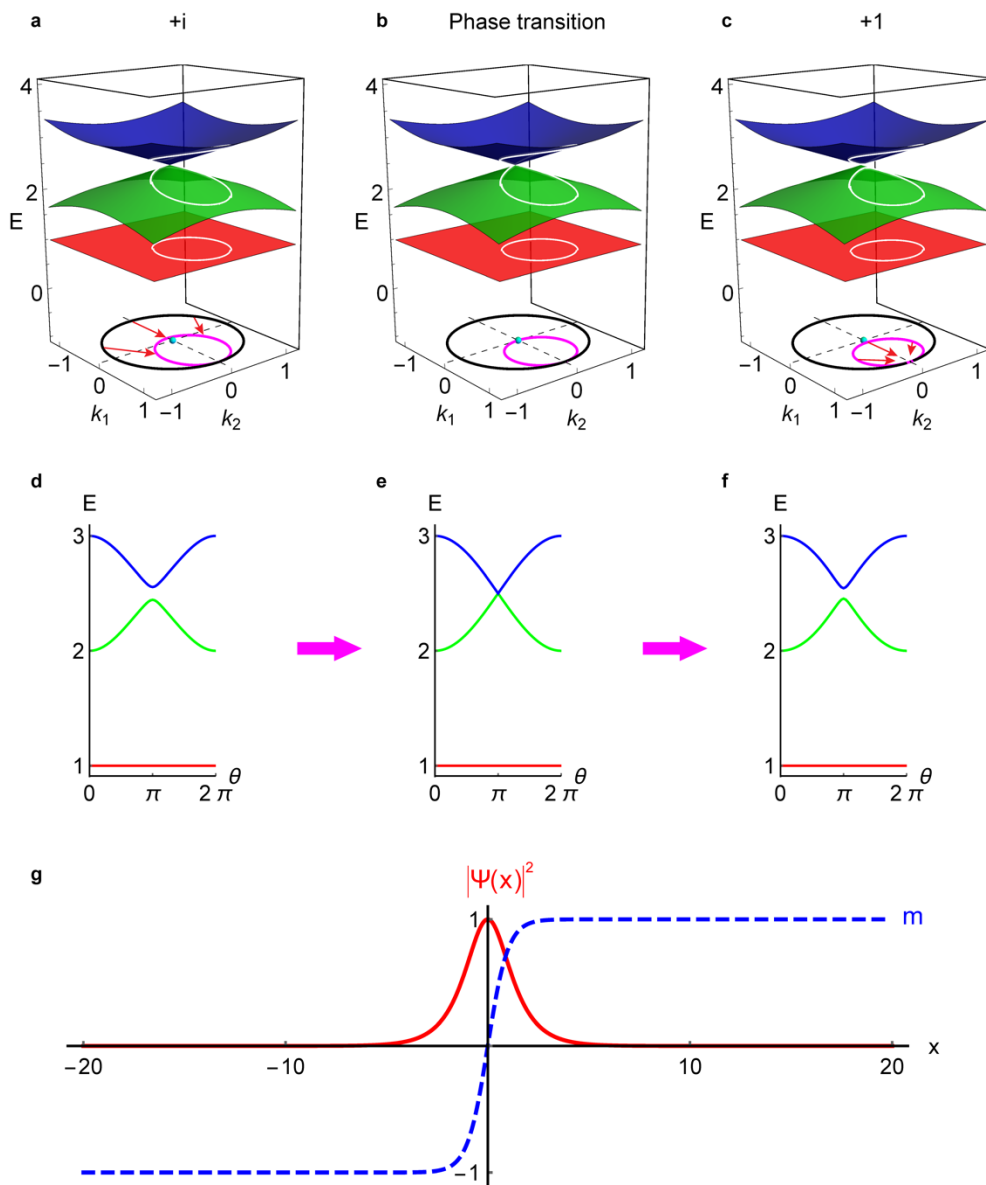
Figure S14 | Jackiw-Rebbi argument for "where there is a bandgap closing there is a domain-wall state". a-c, Topological phase transition from charge $+i$ to $+1$ when continuously shrinking the magenta circle (white circle in each 2D band sheet) via system parameter tuning. **d-f,** The corresponding 1D band structure along the polar angle θ of each magenta circle. The bandgap-closing and reopening imply the existence of edge mode. **g,** Schematically localized domain-wall state between charges $+i$ and $+1$, corresponding to the topological phase transition (b and e).
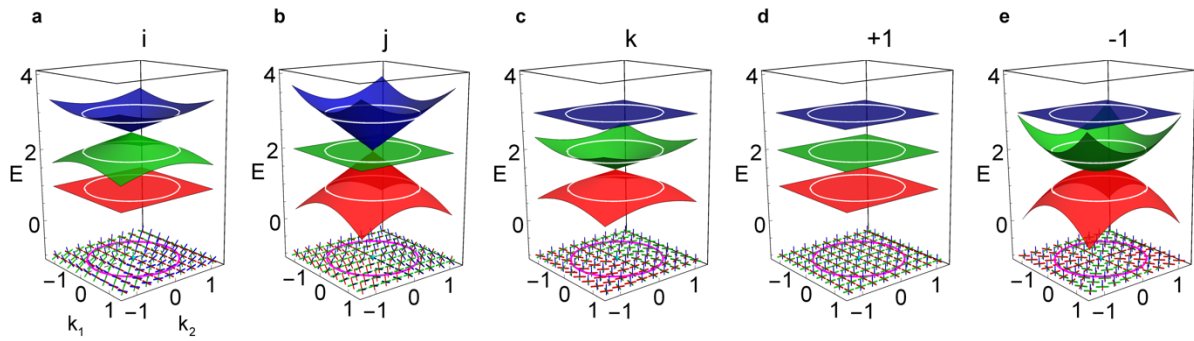
Figure S15 | Extension to 2D extended plane of the flat-band Hamiltonian (parameters are from Tab. S1). The non-Abelian charges are labelled in each panel (a-e). The white unit circle indicates the 1D Hamiltonian (Eq. 2 or Eq. S6). The three bands are coloured in red, green and blue, respectively. The bottom plane indicates the eigenstate distribution.
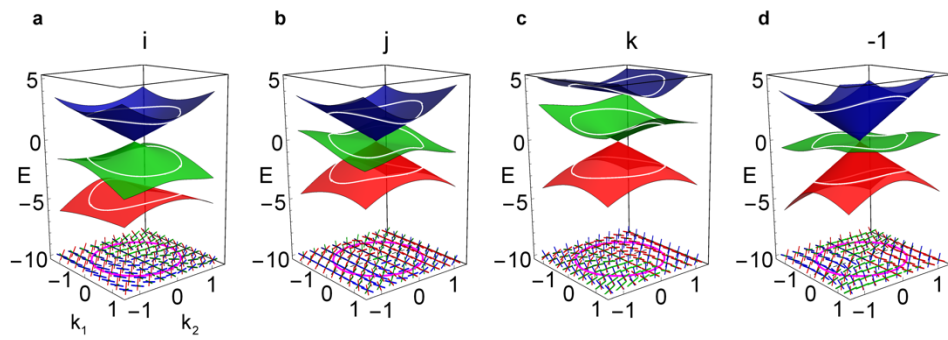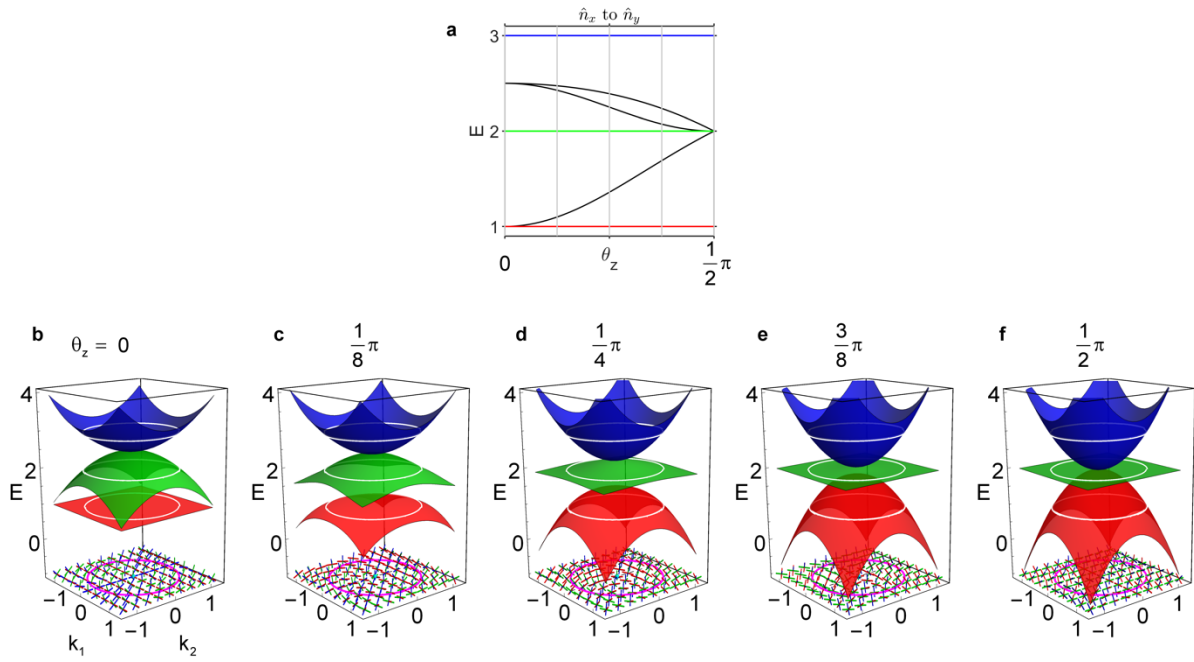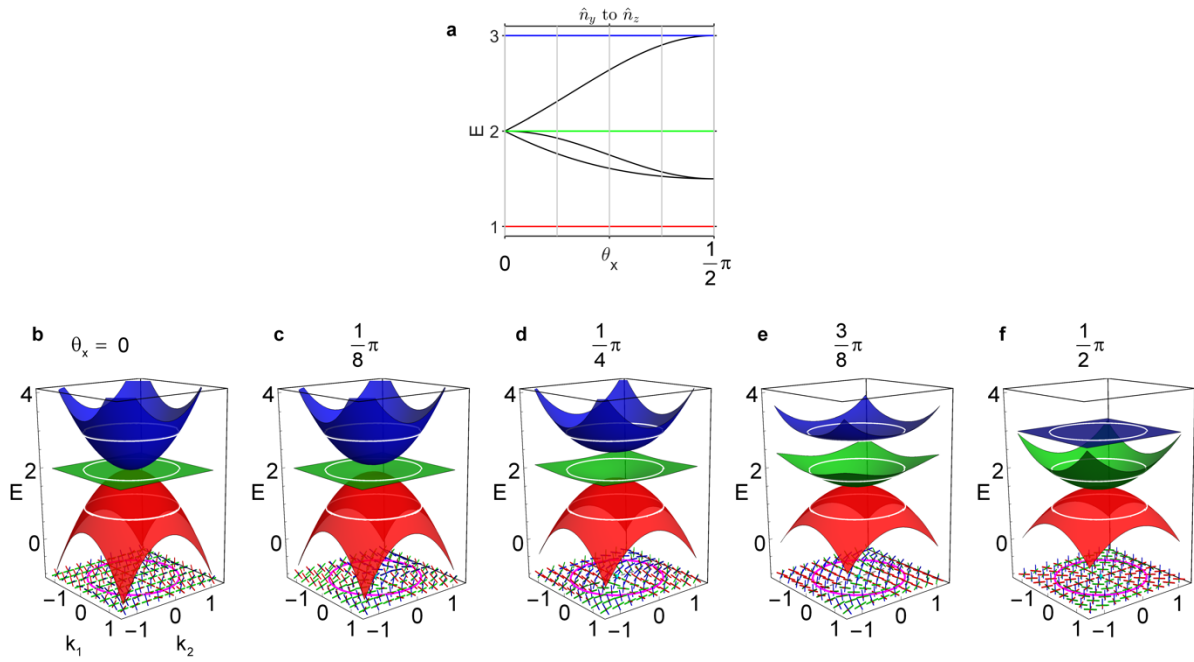
Figure S16 | Extension to 2D extended plane of the Hamiltonian measured in experiment (parameters are from Tab. S2). The non-Abelian charges are labelled in each panel (a-d). The white unit circle indicates the 1D Hamiltonian (Eq. 2 in the main text). The three bands are coloured in red, green and blue, respectively. The bottom plane indicates the eigenstate distribution.

Figure S17 | Extension to 2D extended plane of the flat-band Hamiltonian for charge −1.

a, The edge states (black) evolution with θ_z. With increasing the angle θ_z, the 2D extended bands change from (b) to (f). The white unit circle indicates the 1D Hamiltonian (Eq. S6). The three bands are coloured in red, green and blue, respectively. The bottom plane indicates the eigenstate distribution.
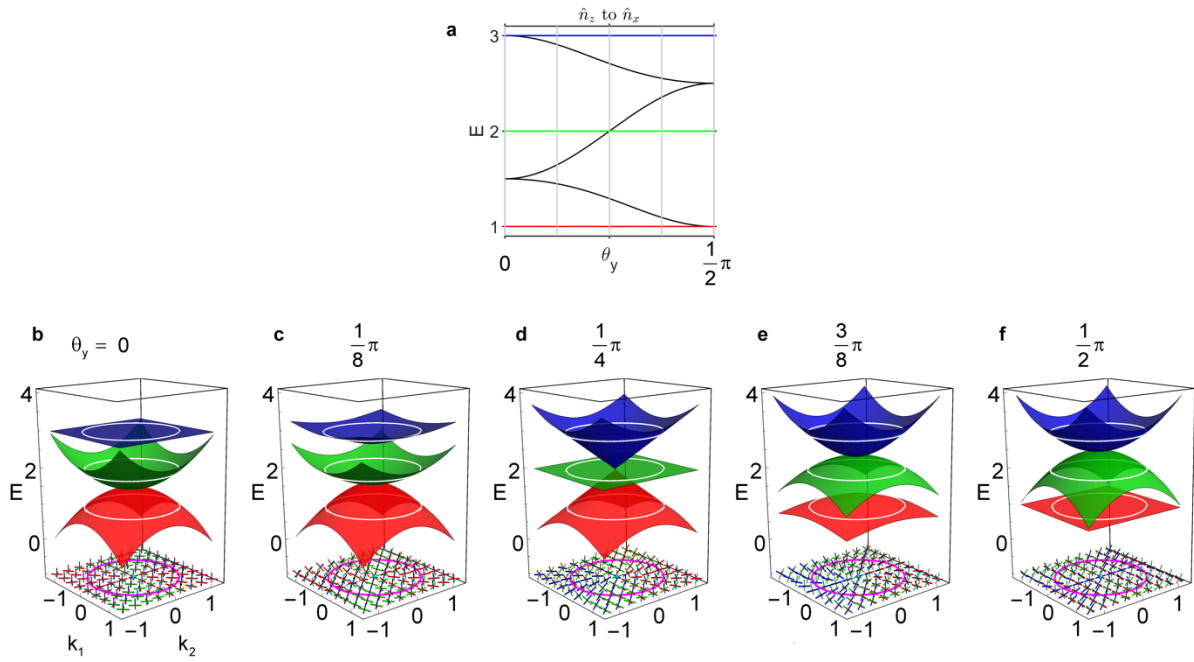
Figure S18 | Extension to 2D extended plane of the flat-band Hamiltonian for charge −1.

a, The edge states (black) evolution with θ_x. With increasing the angle θ_x, the 2D extended bands change from (b) to (f). The white unit circle indicates the 1D Hamiltonian (Eq. S6). The three bands are coloured in red, green and blue, respectively. The bottom plane indicates the eigenstate distribution.

Figure S19 | Extension to 2D extended plane of the flat-band Hamiltonian for charge -1.

a, The edge states (black) evolution with θ_y. With increasing the angle θ_y, the 2D extended bands change from (b) to (f). The white unit circle indicates the 1D Hamiltonian (Eq. S6). The three bands are coloured in red, green and blue, respectively. The bottom plane indicates the eigenstate distribution.
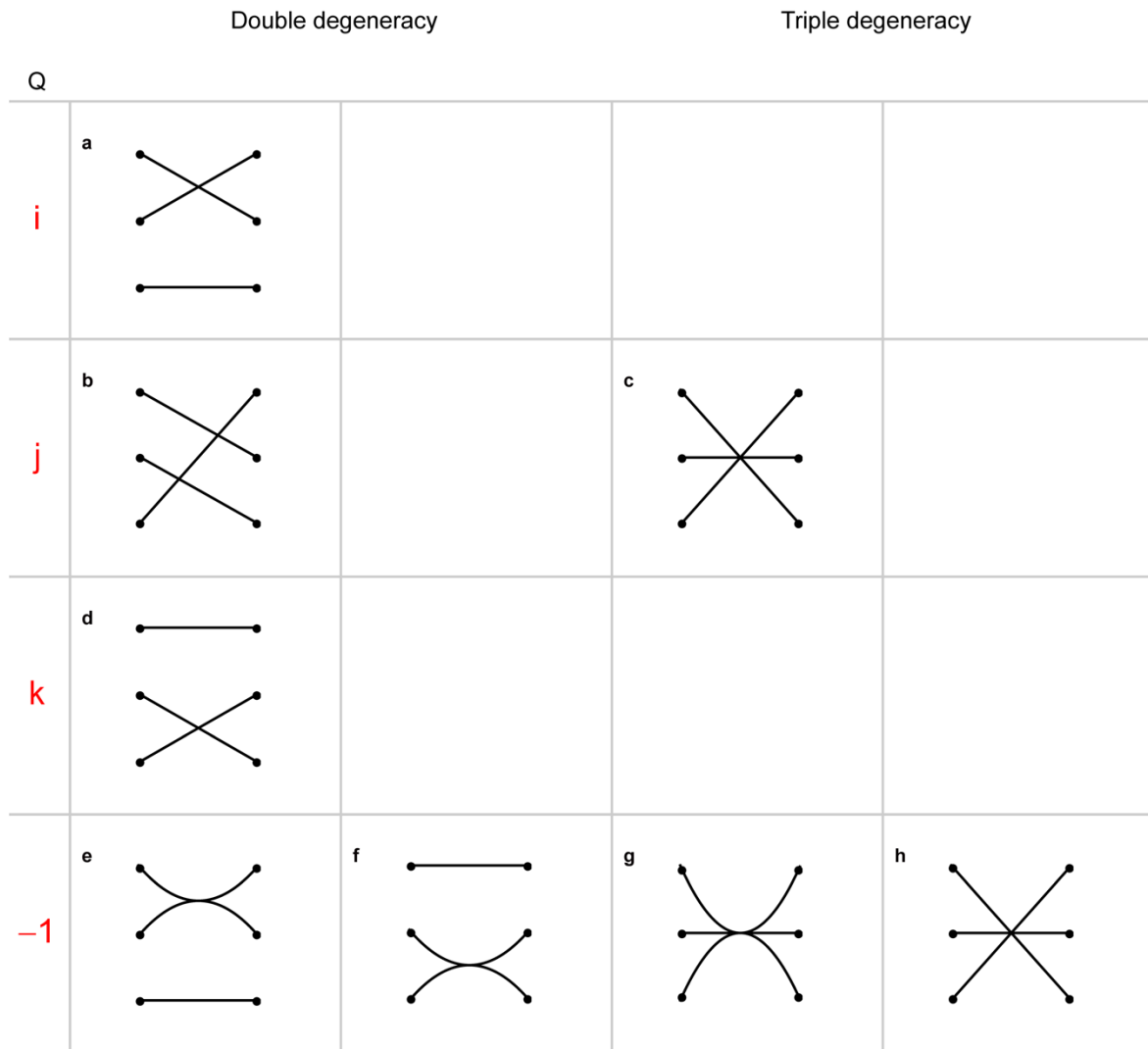
Figure S20 | Summary of band degeneracies in the extended 2D plane for various non-Abelian topological charges. With fixing the left and right end points (black points), one can smoothly adjust the interval bands arbitrarily, i.e., from b to c and mutual transitions between e-h. Here we just show the representative and neat degeneracy forms. The quadratic degeneracies in e-g may split into two Dirac cones.
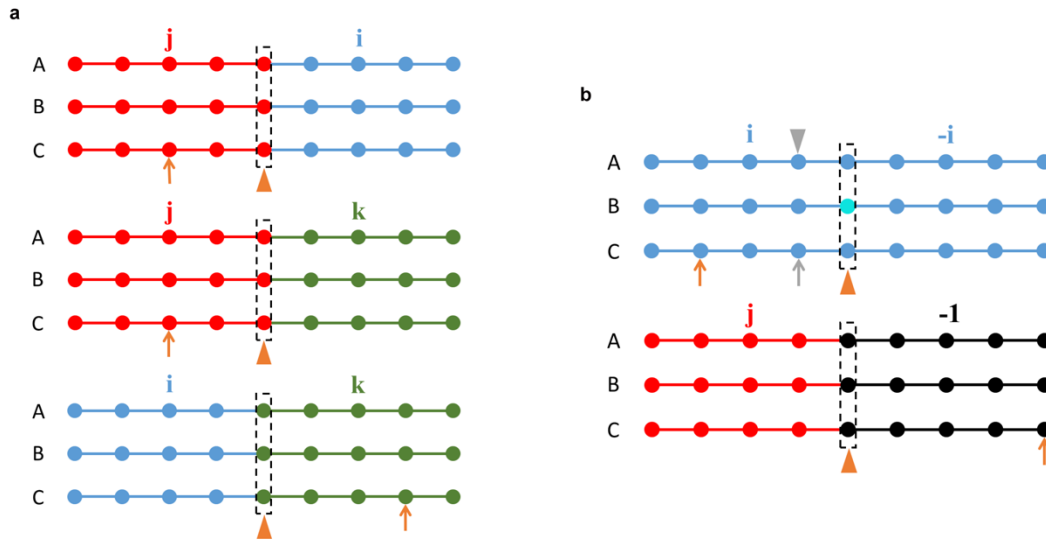
Figure S21 | Domain-wall constructions of different cases measured in experiment, corresponding to Figs. 4d-h in the main text. Arrows/triangles with the corresponding colours are the excitation/probing unit cells of domain-wall states. Dashed boxes indicate the domain-walls, where the onsite energies are chosen from left or right bulk lattices as schematically shown. The domain-wall onsite energies in the charge pair of $(+i, -i)$ are 2, 4 and -4 corresponding to meta-atoms A, B and C, respectively.
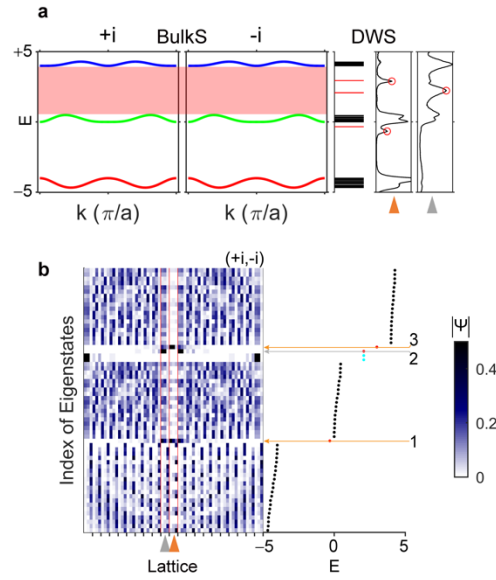
Figure S22 | Field distribution of domain-wall states between charges of $+i$ and $-i$. a, Bulk (BulkS) and domain-wall states (DWS). On the right side the two experimental panels correspond to different probing positions as shown in (b). **b,** Field distribution of the bulk and domain-wall states. Orange/gray triangle indicates the position to probe the (1st and 3rd)/2nd domain-wall states. We note that the domain-wall states can have nearly zero amplitude at some sites.
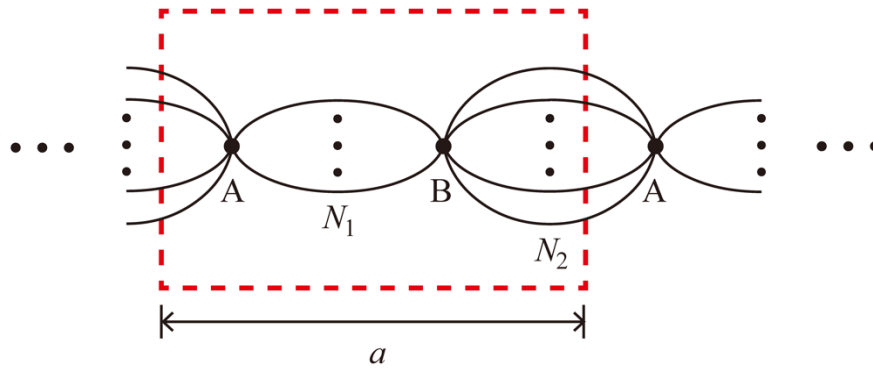
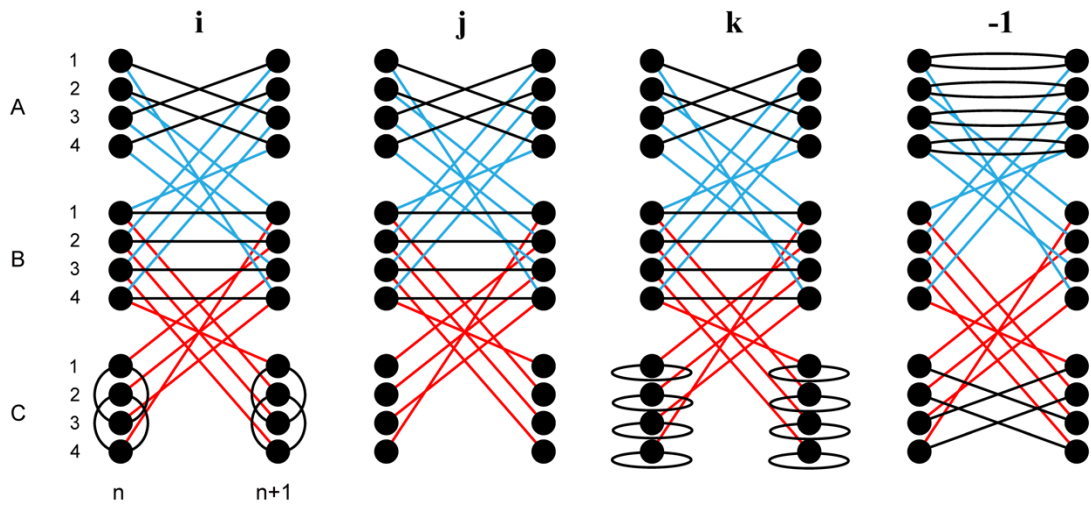**Figure S23 | A one-dimensional periodic transmission line network.**

Figure S24 | Transmission line connectivity of four cases measured in experiments (Fig. 3 in the main text). The corresponding parameters in the tight binding model are listed in Tab. S2.

Figure S25 | Setups for the experimental measurements. 'S' indicates the signal generator (Keysight 8647A Synthesized Signal Generator), and 'O' is the oscilloscope (Keysight DSOX2002A Oscilloscope). The AC frequency signal from the signal generator is input to the nodes of one meta-atom by cable 1 (red arrow). The short cable 2 (cyan arrow) is used to measure the voltage at each node without breaking the original system. The cable 3 (green arrow) is used to provide a reference signal for the phase measurement.